Initial Model Construction for Intermediate-period Full Waveform Inversion of the Contiguous US and Surrounding Regions

submitted to *Geophys. J. Int.*

Initial model construction for intermediate-period full-waveform inversion of the contiguous US and surrounding regions

Tong Zhou [1,3⋆], Ziyi Xi [1], Min Chen [1,2†] and Jiaqi Li [1]

[1] *Department of Computational Mathematics, Science and Engineering, Michigan State University, East Lansing, Michigan,* 48824*, USA.*

[2] *Department of Earth and Environmental Sciences, Michigan State University, East Lansing, Michigan,* 48824*, USA. Corresponding to: chenmi22@msu.edu*

[3] *(now at) Earth Planetary and Space Sciences, University of California, Los Angeles, CA,* 90095*, USA Corresponding to: tzhou@epss.ucla.edu*

SUMMARY

Contiguous US is one of regions well instrumented with broadband seismic stations due to the deployment of the EarthScope Transportable Array. Previous studies have provided various 3D seismic wave speed models for the crust and upper mantle with improving resolution. However, discrepancies exist between these models due to the differences in both data sets and tomographic methods, which introduce the uncertainties of the imaged lithospheic structure beneath North America. A further model refinement using the best data coverage and advanced tomographic methods such as full-waveform inversion is expected to provide better seismological constraints. Initial models have significant impacts on the convergence of full-waveform inversions. However, how to select an optimal initial model is not well investigated. Here, we present a data-driven initial model selection procedure for the contiguous US and

surrounding regions by examining waveform fitting and misfit functions between the observations and synthetics from candidate models. We use a benchmark data set of waveforms from 30 earthquakes recorded by 5,820 stations across the North America. The results suggest that the tested 3D models well capture long-period waveforms while have discrepancies in short-periods especially on tangential components, indicating that the smaller-scale heterogeneities and radial anisotropy in the crust and upper mantle are not well constrained yet. Based on the data fitting, a hybrid initial model combining S40RTS or S362ANI in the mantle and US.2016 for V_{sv} and CRUST1.0 for V_{sh} in the crust is optimal for future full-waveform inversions to achieve higher resolutions of the crust and upper mantle structure.

Key words: model evaluation; waveform misfit; seismic tomography; computational seismology

1 INTRODUCTION

Seismic tomography provides one of the most important physical constraints of the Earth's interior structure and offers insight into the dynamic processes of the lithosphere and asthenosphere. Tomographic images of the Earth's interior, facilitated by large-aperture uniform array deployments (e.g., USArray in North America and CEArray in East Asia) have been tremendously improved in resolution of the crust and upper mantle structure (Yuan et al. 2014; Schmandt & Lin 2014; Chen et al. 2015b; Shen & Ritzwoller 2016; Zhu et al. 2017; Krischer et al. 2018; Tao et al. 2018). Meanwhile, advanced tomographic methods utilizing either multiple data sets (e.g., Shen & Ritzwoller (2016)) or full waveform inversion technique (e.g., Fichtner et al. (2009, 2010); Tape et al. (2010); Lekić & Romanowicz (2011); Yuan et al. (2014); Chen et al. (2015a, 2017, 2019); Zhu et al. (2017); Tao et al. (2018); Krischer et al. (2018)) have helped remarkably in accurately rendering the physical properties of the crust and mantle structure. Although large-scale structures (on the order of thousands of kilometers) in tomographic models of the same regions extracted from different data sets and/or tomographic methods are similarly captured in general, the small-scale structures (on the

* tzhou@epss.ucla.edu
† chenmi22@msu.edu

order of hundreds and/or tens of kilometers) are still very different in terms of both the amplitude and the pattern of seismic wave speed anomalies. These models also have different geometric mesh and inversion parameters, which brings extra complexity for interpretation and use of the tomographic models.

From the inversion aspect, each model has achieved the minimum misfit of the observables on their own data sets. However, if examining the waveform fitting with a uniform and independent validation data set, discrepancies of these model predictions still appear as reported by previous research (Lin et al. 2011; Lee et al. 2014; Gao & Shen 2015; Bao & Shen 2016; Taborda et al. 2016). These discrepancies become more severe when more realistic Earth's properties are taken into account, e.g., the topography, attenuation, and the Earth's ellipticity. Therefore, it is important to further refine the seismic wave speeds model of contiguous US and surrounding regions within a full-waveform inversion framework that takes more realistic Earth properties and larger waveform data sets into consideration.

Full-waveform inversion methods usually minimize the data-synthetics misfit iteratively with gradient-based methods (Tromp et al. 2005), which is highly nonlinear and depends on the initial model. A good initial model is reported to be helpful to prevent the inversion from being trapped into a local minimum (Mulder & Plessix 2008; Fichtner et al. 2009; Bozdağ et al. 2016; Zhu et al. 2017; Krischer et al. 2018; Zhou et al. 2019). FWI studies usually have their own preference in selecting initial models, e.g., a 1D mantle model with 3D crust (Lekić & Romanowicz 2011), a global 3D mantle model with a global crustal model (Chen et al. 2015a; Bozdağ et al. 2016; Zhu et al. 2017), a hybrid model combining 3D regional mantle and crustal models (Krischer et al. 2018), or a combination of previous FWI models (Yuan et al. 2014; Tao et al. 2017). The effect of crustal models is also addressed (Bozdağ & Trampert 2008; Ritsema et al. 2009; Ferreira et al. 2010), showing that a better crustal model is also the key to the inversion. The initial model selection generally requires better data fitting to satisfy the linearlize approximation and less artifacts to influence the further iterations. However, this issue is not systematically and quantitatively discussed.

The contiguous US is one of the most instrumented continental-scale regions that are extensively investigated by many tomographic studies (Engdahl et al. 1998; Bedle & van der Lee 2009; Schmandt & Humphreys 2010; Lin et al. 2012, 2014; Pavlis et al. 2012; Porritt et al. 2014; Schmandt & Lin 2014; Yuan et al. 2014; Schmandt et al. 2015; Shen & Ritzwoller 2016; Buehler & Shearer 2017; Burdick et al. 2017; Zhu et al. 2017; Jiang et al. 2018; Krischer et al. 2018; Nelson & Grand 2018) with different data sets and tomographic methods. This provides

us a good example of examining different regional and global models to discuss a standard procedure for selecting initial models for FWI inversions.

As reported by other studies (Alex Song & Helmberger 2007; Qin et al. 2009; Bozdağ & Trampert 2010; Gao & Shen 2012; Lee et al. 2014; Gao & Shen 2015; Maceira et al. 2015; Bao & Shen 2016; Taborda et al. 2016), it is effective to compare tomographic models by examining the misfit of observed and predicted waveform with 3D numerical simulation. These comparisons suggest that traveltime tomographic models generally recover the pattern of wave speed variations but not the full wave speed contrast and thus are unable to reproduce accurate waveform distortions (Alex Song & Helmberger 2007), while new tomographic models utilizing more data coverage and/or full waveform inversion methods tend to have better predictability of the waveforms (Gao & Shen 2012, 2015). However, the predictability of tomographic models under realistic conditions including attenuation, topography, gravity, ellipticity, etc. is still unknown. Such predictability not only tells the compatibility of these models to a realistic configuration of numerical waveform simulation, but also serves as an indication for selecting initial model for FWI with realistic properties taken into consideration.

In this work, we aim at building a procedure of initial model selection by comparing the waveform fitting of several recent shear wave speed models of the contiguous US and surrounding regions. The waveform fitting between synthetics and observations for each model is systematically analyzed using an independent earthquake event set and a spectral-element method (SEM) based wave equation solver SPECFEM3D_GLOBE (Komatitsch & Tromp 2002a,b) with the consideration of topography, attenuation, gravity, and Earth's ellipticity. We investigate multiple misfit functions which are widely used in FWI approaches, including the travel time misfit, amplitude misfit, waveform misfit (Tromp et al. 2005) and the normalized zero-lag cross-correlation coefficient (NZCC) misfit (Tao et al. 2017) of body and surface waves in intermediate period ranges. Especially, the NZCC is sensitive to both arrival time and waveform similarity between data and synthetics, which is more indicative of the model's predictability for seismic data than the commonly used criterion of travel time misfit derived from cross correlation.

In the following sections, firstly, we introduce the seismic models selected for comparison. Then we systematically compare the waveforms and statistical result of misfit functions for different models in three different intermediate period ranges, 9-20 s, 20-40 s, and 40-120 s. Lastly, we discuss the effectiveness, difficulty, and insight of the initial model selection based on model comparison.

2 DATA AND METHODS

2.1 Seismic models for comparison

Since P waves are generally better predicted than S waves, in this study, we focus on analyzing shear wave speed models. Here we present seven publicly available models which have the resolution for the contiguous US and surrounding regions, including a differential travel-time tomographic model US-SL-2014 (Schmandt & Lin 2014), an ambient noise and receiver function jointly inverted model US.2016 (Shen & Ritzwoller 2016), two FWI models SEMum-NA14 (Yuan et al. 2014) and Krischer18 (Krischer et al. 2018), and three global tomographic models GyPSuM (Simmons et al. 2010) inverted from travel times and geodynamic constraints, S362ANI and S40RTS (Kustowski et al. 2008; Ritsema et al. 2011) both constrained by travel times, long period body waves, and surface wave dispersion. The global 1D model AK135 (Kennett et al. 1995) is also selected as a reference to compare with the 3D models. The method and data set used for each model are briefly summarized in Table 1.

All 3D models share similar large-scale pattern of shear wave speed anomalies in the upper mantle (Fig. 1), i.e., relatively low wave speeds (low-V) in the western US and relatively high wave speeds (high-V) in the central and eastern US. However, the small-scale anomalies of tens or hundreds of kilometers differ dramatically in terms of not only the anomaly pattern but also the amplitude, which are caused by different datasets and methods used in the tomographic studies. For example, models US-SL-2014, US.2016, and Krischer18 clearly capture the Yellowstone hotspot in the northwestern US, while the other three miss this small-scale feature possibly due to the lack of resolution because of either sparse data coverage or long-wavelength seismic waves used in the inversion. It is notable that the full waveform inversion model Krischer18, although derived from long-wavelength seismic waves, can already capture small-scale structures such as the Yellowstone hotspot track. This further indicates that the full waveform inversion has the advantage of achieving sub-wavelength resolution (van der Kruk et al. 2015). However, in the case of lacking high-frequency data coverage, full waveform inversion is still unable to recover some small-scale structures compared to traditional asymptotic methods but with more suitable data sets. For example, in Pacific Northwest, the Cascadia slab shows up as elongated narrow and strongly high-V anomalies in model US-SL-2014 because short-period teleseismic body wave travel time data enhances the lateral resolution of the structures at such scale. On the other hand, the FWI model Krischer18, although based on a more accurate 3D sensitivity kernel, does not well capture the narrow

high-V Cascadia slab due to the lack of short-wavelength teleseismic data that can sample the slab with good azimuthal and incidence angle coverage.

Besides the differences in data sets and tomographic methods, crustal models used in the seismic inversion can also lead to dramatic differences between mantle models. An accurate crustal model is critical for correctly recovering deeper structure, especially the uppermost mantle which is more sensitive to the tradeoff with the wave speeds in the crust (Bozdağ & Trampert 2008; Panning et al. 2010). Figure 2 shows the absolute shear wave speeds at 20 km depth for three different crustal models resulted from inversions of models GyPSuM, US.2016, and Krischer18, along with the widely used 3D crustal model, CRUST1.0 (Laske et al. 2013). The average shear wave speed difference amongst the crustal models within the contiguous US reaches up to 10%, e.g., about 3.3 km/s beneath the Pacific Northwest in model Krischer18 compared to about 3.7 km/s in model US.2016, and an average of 3.5 km/s beneath the central and eastern US in model Krischer18 compared to 3.9 km/s in model CRUST1.0. The impact of the crust and uppermost mantle on the predicted waveforms will be discussed in the following sections.

2.2 Spectral-Element Method and Model Implementation

The predictability of the selected 3D models is evaluated by comparing the observed waveforms with the synthetic waveforms calculated by the SPECFEM3D_GLOBE solver based on the spectral-element method (SEM) (Komatitsch & Tromp 2002a,b). The SEM combines the accuracy of pseudo-spectral method and the flexibility of finite-element mesh (Komatitsch & Tromp 2002a), which honors the topography/bathymetry and any laterally varying internal discontinuities of the Earth such as Moho, 410 and 660 discontinuities. It is more accurate in simulating surface waves than finite-difference methods which have stronger numerical dispersion issue (Robertsson 1996). The effects of Earth's ocean gravity, ellipticity, 3D complex heterogeneity, attenuation, and anisotropy on seismic wave propagation can also be accurately modeled (Komatitsch & Tromp 2002b).

The SEM mesh in this study is designed to simulate seismic waves accurately to the shortest period of 9 s, with a horizontal grid spacing of 5 km between Gauss-Lobatto-Legendre points in the crust and doubled in the mantle. The computational domain is a spherical chunk from the surface to the core mantle boundary, laterally spanning the entire contiguous US, Mexico, and majority of Canada, with horizontal dimensions of $48^\circ \times 48^\circ$ along great circles centered at (99° W, 30° N) and rotated by 30° counterclockwise (Fig. 3a) with Stacey absorbing boundary condition applied at the edges of the computational domain.

The implementation of different models in the SEM mesh is challenging for completely fair model comparison. First, the models cover different study regions and have different parameterizations, which requires to fill the gaps in the unresolved region (e.g., the Mexico region) and unresolved wave speed (e.g., V_p) in the computational domain. Second, each model is inverted with different configurations, e.g., attenuation, topography, radial anisotropy, etc. These two main obstacles make it extremely difficult to accurately compare the data predictability of all the tested models. However, for the purpose of constructing an initial model for FWI, we will focus on the compatibility of each model with the pre-defined model configuration of FWI. Therefore, the models are implemented with the same mesh configuration, topography, radial anisotropy, and attenuation regardless their original set-up.

The compatibility of crustal and mantle models need special attention. For models with only the mantle resolved, we implement model Crust1.0 in the crust because we would like to test the compatibility of those mantle models with this most updated global crustal model, even if some of the global models (e.g., S40RTS and S362ANI) applies Crust2.0 for crustal correction in their inversion. For model US.2016, we implemented its own crust with their Moho by stretching the wave speeds according to the Moho and surface topography.

Some model does not constrain the P wave speed. For those models, a constant Vp/Vs ratio, 1.73, is applied to assign Vp. Density ρ is assigned using 1D reference model AK135. The SEM mesh enables radial anisotropy to account for the models with radial anisotropy parameterization (SEMum-NA14 and S362ANI). For the isotropic models, the V_{sv} and V_{sh} are assigned with the same isotropic shear wave speed V_s for the model implementation. The Q value is set to be PREM Q in the mantle and constant Q=600 in the crust. The implementation details for each model is described in Text S1 in the supplementary material.

2.3 Independent Test Data Set

A total of 30 earthquakes are selected from the global centroid moment tensor solution catalog (Ekström et al. 2012) based on their large number of high-quality waveforms with high Signal-to-Noise Ratio (SNR) and representative geographic coverage of the simulation region (Fig. 3(a)). These events are from 2006 to 2019 with moment magnitude between 4.9 to 6.7. The depth of these events are mostly within the crust, and only two of them are deeper than 30 km. 16 are located within the contiguous US. We used all the broadband stations available from different data centers such as IRISDMC, SSN and CNDC, with a total number of 5,820, shown in Figure 3(b). On average, there are more than 500 stations available for each event.

To process the data, we first remove the instrument response and convert the records

to displacement with a wide-band frequency taper as the pre-filter, and then check the data signal-to-noise ratio and select all traces with SNR>4. Then we band-pass filter the waveforms to our interested frequency ranges with a zero-phase fourth-order Butterworth filter. Finally, both the data and the synthetics on E and N components are rotated to the radial and tangential (R and T) components according to the back azimuth. The synthetic waveforms follow exactly the same procedures of pre-processing as the observed data.

Given that the long-period tomographic models (e.g., SEMum-NA14 and S40RTS) utilize long-period body waves starting at 40 seconds, we choose two period ranges of 20-40 s and 40-120 s to assess the intermediate period and long period waveform fitting of the models. The waves of 9-20 s are also considered to test the waveform fitting in shorter period range.

2.4 Misfit Measurements between Data and Synthetics

We apply four different criteria in this study to evaluate the waveform fitting between the data and synthetics: travel time misfit, amplitude misfit, least-squares waveform misfit, and the waveform similarity measured by the normalized zero-lag cross-correlation coefficient (NZCC). The travel time misfit for a single measurement is defined as the square of the travel time difference between data and synthetics measured by cross-correlation in the selected time window (Tromp et al. 2005):

$$\chi_r^T = \frac{1}{2}[T_r^s - T_r^d]^2, \tag{1}$$

where T_r^s and T_r^d are the measured travel time of the synthetics and data of a specific phase at station r. The amplitude misfit for a single measurement is defined as (Tromp et al. 2005):

$$\chi_r^A = \frac{1}{2}[A_r^d/A_r^s - 1]^2, \tag{2}$$

where A_r^s and A_r^d are the measured amplitude of the synthetics and data of a specific phase at station r. The waveform misfit for a single measurement is defined as (Tromp et al. 2005):

$$\chi_r^F = \frac{1}{2}\int_{t_s}^{t_e} [s(x_r,t) - d(x_r,t)]^2 \mathrm{dt}, \tag{3}$$

where $s(x_r,t)$ and $d(x_r,t)$ are the synthetic and data waveforms at the station r (with location x_r). t_s and t_e are the start and end time of the selected time window.

Besides above-mentioned misfit functions, we also consider the normalized zero-lag cross-correlation coefficient (NZCC), which best reflects both the phase match and the similarity of complex waveform shape, e.g., for triplicated waveforms but without considering the absolute

amplitude. It has been used as an objective function for full waveform inversion which more robustly recovers seismic structures with strong wave speed contrasts than using frequency-dependent travel time misfit (Liu et al. 2016; Tao et al. 2017, 2018). The NZCC is defined as:

$$\mathrm{NZCC} = \frac{\int_{t_s}^{t_e} s(x_r, t) \cdot d(x_r, t) dt}{\sqrt{\int |s(x_r, t)|^2 dt \int |d(x_r, t)|^2 dt}} \tag{4}$$

where $s(x_r, t)$ and $d(x_r, t)$ are the multi-component synthetics within the measurement time window at station r. For the P, SV and Rayleigh waves, the vertical (Z) and radial (R) components are used for calculating NZCC, while for the SH and Love waves, only the tangential (T) component is used.

To make comparison fair, we use fixed time windows for different models, which are selected according to the travel time predicted by 1D model AK135 for body wave phases, and constant speeds for surface wave phases (Table 2). For intermediate and long period ranges, S waves are merged with the surface wave train at local epicentral distances ($\Delta < 10^\circ$). Therefore, for local epicentral distances, only P(Pnl) and surface wave windows are selected, while P, S, and surface wave windows for $\Delta \geq 10^\circ$ are selected. The P and S windows are selected 10 s before and 60 s after the predicted arrival time. On the other hand, the surface wave windows are 10 s before and 120 s after the predicted arrival time of the surface wave train. The measurement windows are then fine selected by the following criteria: (1) the signal-to-noise ratio of the data (SNR>4) and (2) the cross-correlation coefficient of the data and synthetics (CC>0.7).

The misfit function for a model combines all the measurements for selected measurement windows for each event-station pair. We apply the same categorical weighting scheme as previous FWI studies (Tape et al. 2010; Chen et al. 2015a; Zhu et al. 2017) to make our model assessment consistent with FWI workflow for initial model selection. The categorical weighting separates all the measurements to six categories: body waves and surface waves on Z, R and T components, respectively. This scheme balances different number of measurements on each components and each category of seismic phases, i.e., body and surface waves. Since the station distribution is highly biased and varies for different events (e.g., a dense local network with 10-km station spacing such as SCEDC, compared to the USArray with average station spacing of 70 km), it is important to apply a proper weighting scheme to account for the biased station distribution for each event in evaluating the overall predictability of each model. For each testing event, we applied the station weighting based on their geographical distribution (Ruan et al. 2019). To make the measurements of different windows comparable,

we normalize the travel time misfit and the amplitude misfit by the standard deviation of their measurement, i.e.,

$$\chi^T = \frac{1}{2CN}\sum_c^C\sum_r^N W_c W_r \left(\frac{T_r^s - T_r^d}{\sigma_r}\right)^2, \tag{5}$$

$$\chi^A = \frac{1}{2CN}\sum_c^C\sum_r^N W_c W_r \left(\frac{A_r^d/A_r^s - 1}{\sigma_r}\right)^2, \tag{6}$$

where W_r is the geographical station weighting coefficient (Ruan et al. 2019) and W_c is the category weighting coefficient, which is the inverse of the number of all the selected measurement time windows of that category. σ_r is the estimated error of the measurement, calculated by the MEASURE_ADJ incorporated in the SPECFEM3D_GLOBE code package (Komatitsch et al. 9999). C and N are the numbers of total categories and stations, respectively. In the waveform and NZCC measurements, we only apply the categorical and geographic weighting:

$$\chi^F = \frac{1}{CN}\sum_c^C\sum_r^N W_c W_r \chi_r^F \tag{7}$$

$$\chi^{\mathrm{NZCC}} = \frac{1}{CN}\sum_c^C\sum_r^N W_c W_r (1 - \mathrm{NZCC}) \tag{8}$$

where W_r and W_c are the geographical and categorical weighting, respectively.

The uncertainty of source parameters also has impact on the waveform fitting measurements. Here we apply a combination method of CMT3D (Liu et al. 2004) and the grid-search of Rayleigh wave spectra (Jia et al. 2017) to re-invert for the moment tensor and event depth (Text S2 and Fig. S1). The example of earthquake event 200802211416A (Mw 6.0) shows a slight depth decrease and a better amplitude misfit for Rayleigh waves.

3 RESULTS

3.1 Waveform Comparison of Different Seismic Models

To visualize the waveform fitting, we choose an earthquake event 201305240347A (Mw 5.7) and stations located towards east in azimuth range of 90±10° (Fig. 3(c), vertical cross-section: Fig. S2). We demonstrate waveform comparisons of intermediate period shear waves (20-40 s, Fig. 4) and long period surface waves (40-120 s, Fig. 5) in vertical and tangential components. The intermediate period shear waves merge with the surface waves within epicentral distance ranges of 10° (Fig. 4), therefore, only surface wave windows are plotted for the local epicentral distance stations. The turning depth of the S-wave ray ranges from 35 - 816 km, mostly sensitive to the upper mantle.

All the models fit the regional SV and SH phases well (Fig. 4). Models derived with full-waveform tomography, e.g., Krischer18 and SEMum-NA14 seems to have better waveform fitting and smaller travel time misfit on vertical components. On the other hand, models with radially anisotropic constraints, e.g., S362ANI and SEMum-NA14 performs better on tangential components. The models all have a larger phase shift for local Rayleigh waves but performs better for local Love waves. In general, all the models are consistent in well predicting the waveforms longer than 20 seconds, and are compatible with the SPECFEM3D_GLOBE mesh configurations.

Surface waves in long period range of 40-120 s are most sensitive to the upper mantle structure. Here, Rayleigh waves on vertical components are well predicted by all the tested models (Fig. 5) and amongst which, model US.2016 has the smallest Rayleigh wave phase misfit. However, models AK135, US.2016 and US-SL-2014 have relatively large phase misfit of the Love waves. Interestingly, global models S362ANI, and even S40RTS which does not have radial anisotropy constraint, manifest a better Love wave fitting which is partially due to the better compatibility of crustal and mantle models implemented (see discussion). This observation suggests that radial anisotropy in the upper mantle still needs to be refined.

Waveforms in the short period range of 9-20 s are most sensitive to the small scale heterogeneities in the crustal structure. However, relatively large body and surface wave misfits for all the models in 9-20 s are observed (Text S3, Fig. S3 and S4). Currently, none of the models can predict the waveform complexities of the shortest period around 9 s. For body waves, models US.2016, S40RTS and US-SL-2014 have a slightly better waveform fitting (Fig. S3). The short period surface wave observation is complicated with strong coda reverberations (Fig. S4), which may be related to reverberations triggered by the deep sedimentary basins (e.g., Forest City, Cherokee and Illinois (Coleman Jr & Cahan 2012), Fig. S2). The small-scale heterogeneities in the shallow sub-surface also need further refinement.

We demonstrate the impact of different crustal models to the intermediate-period (20-40 s) waveforms in Fig. 6. The earthquake event 200802211416A (Mw 6.0) recorded by one global seismic network station IU.CCM with epicentral distance 18° is used. Three different crustal models, Crust1.0, Crust2.0 and US.2016 are implemented along with the same mantle model S40RTS. All the models predict P and SH waves well, while model S40RTS with Crust2.0 has smaller waveform misfits. For SV and Rayleigh waves, S40RTS+US.2016 has the best waveform fitting, while for Love waves, S40RTS+Crust1.0 has the best prediction. This observation suggests that the original compatible crustal and mantle models (e.g., Crust2.0 for S40RTS) generally predicts the same types of data used in their inversion, but are not optimal

for the other types of data. A crustal model with higher resolution (e.g., Crust1.0) or with short-period Rayleigh wave dispersion constraints (e.g., US.2016) has a visible improvement on the waveform fitting of certain seismic phases such as SV waves and Rayleigh waves.

3.2 Statistical Result of Waveform Similarity and Misfit

Statistical analysis helps us assess the compatibility of the models with the contiguous US mesh configuration in terms of waveform fitting. First, travel time shift histograms directly indicate the mean and deviation of each model (Fig. 7). The positive or negative travel time indicates advance or delay of the synthetics compared to the observations, implying that the wave speed models are either faster or slower compared to the ground-truth models. We observed that model S40RTS and S362ANI have the minimum standard deviation in all three period ranges, which is likely because that the two global models completely cover our entire study region and are unlikely subjected to the bias introduced by composite models that require multiple incompatible models to fill up the entire simulation domain. Model GyPSuM, Krischer18 and US.2016 has the lowest mean travel time error for 9-20 s, 20-40 s and 40-120 s, respectively. All the models have a negative mean travel time shift in 9-20 s and 40-120 s, while only GyPSuM and Krischer18 have positive travel time shift in 20-40 s period range. The observed biased shear wave travel time misfit is likely due to the surface topography effect. The top layer of each model is stretched to fit the surface topography above the sea level in the contiguous US, but this layer usually have faster wave speed than a realistic near-surface sedimentary layer. Measurements with only body waves or surface waves share similar statistical results (Figs. S5 - S8 in the supplementary). SH wave speeds for all the models seem to systematically slower (Fig. S6), while the Love wave speed (Fig. S8) show less systematically biased distribution, indicating the mantle radial anisotropy need further refinement (Text S4). Amongst these models, models SEMum-NA14 and S362ANI have better performance in predicting seismic waves on different components, probably due to the radial anisotropy is constrained in these two models.

Besides the statistical analysis, we examine the averaged travel time shift of all the available events at each station, which shows the waveform fitting in different geographic regions. Fig. 8 shows the shear wave travel time misfit in the intermediate (20-40 s) period range for all the tested models. Generally, the absolute travel time misfit in the western US is slightly larger than the eastern US, indicating the western US has more complex and unresolved structures. The Rocky Mountain and Plateau region has relatively large shear wave misfit while for the Great Plain region relatively small, possibly due to the large topography effects in

the Rocky Mountain and Plateau region. The global models S40RTS, GyPSuM and S362ANI have a relatively small misfit in the Eastern US than the other models, which may indicate that these global models well capture the average large-scale structures in the Eastern US.

We examine the compatibility of each model with our FWI mesh configuration by a variety of misfit functions (Fig. 9) The travel time misfit and NZCC misfit share similar trend of ranking, which is because of the NZCC misfit measures the phase difference which is coherent to the travel time misfit. Models S40RTS, S362ANI and US.2016 are the top three models with minimal overall travel time misfit and NZCC misfit in 20-40 s and 40-120 s period ranges, while in 9-20 s period range, model AK135 becomes one of the top three instead of US.2016. Global models constrained by both the travel time data (short period) and surface wave dispersion data (long period) has the smallest misfit of phase for both the body and the surface wave in different frequency ranges. Measurements with body waves or surface waves share similar statistical results as the ones of all the seismic phases combined (Figs. S9 and S10 in the supplementary material).

For the amplitude and waveform misfits with longer periods, both of them have a similar trend of model ranking as travel time and NZCC misfit, while in the short period range the amplitude and waveform misfits are more unpredictable. The amplitude and waveform misfits may not be very indicative of model predictability because none of the tested models are inverted using absolute amplitude or waveform misfits. The short period surface waveforms are not well predicted at all by all the models because none of them has a good constraint of the very shallow sub-surface structure such as the sedimentary basins. The long period surface waves are less subjective to the strong and small-scale heterogeneities in the shallow depths, therefore, the amplitude and waveform misfits are more indicative in assessing the model predictability for long periods. Further refinement for near-surface small scale heterogeneities is still needed for seismic wave speeds models of contiguous US and surrounding regions.

Using NZCC, we can determine the percentage of windows selected for measurement from all the possible windows. It is an important criterion that directly indicates the number of usable measures we can obtain in typical FWIs, thus indicative for initial model predictability. Here, we plot the percentage of measurement windows with NZCC>0.7 for all the models in three period ranges and six categories (Fig. 10). To make comparison fair, we examine only contiguous US earthquakes including events off coast western US because models US.2016 and US-SL-2014 only have contiguous US part resolved. For the short period range (i.e., 9-20 s), models S362ANI, S40RTS and GyPSuM are the three models with higher percentage of usable measurement windows of body waves, while model US.2016, US-SL-2014 and

Krischer18 have higher percentage of usable windows of Rayleigh waves. For love waves, model AK135+Crust1.0 predicts the waveforms better than model US.2016, which indicates that Crust1.0 is more suitable for SH waves in the crust. For the long period range (40-120 s), models S40RTS, S362ANI and SEMum-NA14 are the top three models with the highest percentages of usable windows for all six categories, which further confirms that the predictability of certain types of waves is highly dependent on the data used in the inversion, e.g., the long-period waveforms used in these three models. In the intermediate period range (20-40 s), models S40RTS and S62ANI are amongst the best three models with the highest percentages of NZCC>0.7 measurement windows for all the categories, while SEMum-NA14 and Krischer18 also predict well for some categories. The overall percentage of good measurements increases with increasing periods.

The model predictability varies with the epicentral distance in each category (Fig. 11). For surface waves, the predictability of all the models decays with increasing epicentral distances, which may be contributed by the small-scale heterogeneities in the crust and uppermost mantle. Such heterogeneities are not well constrained by the current models thus complex surface wave dispersion at increasing epicentral distances cannot be fully reproduced. Model US.2016 performs the best for short period (9-20 s) Rayleigh waves in all the epicentral distances, indicating a relatively better constrained shallow subsurface structures. Models with Crust1.0 (S40RTS, US-SL-2014 and SEMum-NA14) performs better in fitting short period Love waves, which further confirms that Crust1.0 serves a good model for SH wave speeds in the crust of the contiguous US and surrounding regions. Models S40RTS and S362ANI are amongst the best fitting models in periods greater than 20 s, while models Krischer18 and SEMum-NA14 also show good predictability especially at larger epicentral distances. For body waves, models S40RTS and S362ANI generally outperforms other models, especially at large epicentral distances. We also noticed that model AK135 predicts 9-20 s shear waves at small epicentral distance well, however the composite model with Crust1.0 and AK135 worsens the waveform fitting, which is consistent with the previous study on that adding 3D crust does not necessarily improves the data fitting for 1D models (Bozdağ & Trampert 2010).

4 DISCUSSION

4.1 Uncertainties and Assessment of the Data Misfit for Model Comparison

Uncertainties of the data misfit come from various aspects. Firstly, the incompleteness of the parameters and the composite model implementation made of multiple incompatible models

lead to the bias or artifacts in the waveform simulations. Therefore, assessing the model predictability based on the waveform comparison result need to be carefully discussed. Body waves in regional epicentral distances (10-30°) are sensitive to the upper mantle structure, while in local epicentral distances sensitive to the crustal structure, e.g., Crust1.0. Therefore, it is important to analyze the NZCC statistics by taking into account of epicentral distances (Fig. 11), the waves of which are sensitive to models at different depth ranges.

The data sets used in their inversion of each model determines the data fitting in each category. For example, model US.2016 with short period Rayleigh wave dispersion data recorded by USArray significantly improves the waveform fitting of 9-20 s Rayleigh wave, resulting in a better crustal isotropic shear wave speed model. Models Krischer18 and SEMum-NA14, both FWI models with long period (30-40 s) body and surface waves used in their inversion, are able to predict the long period (40-120 s) validation data sets and even for the intermediate period (20-40 s). The FWI approach maximizes the information extracted from the seismic waveforms, which may have sub-wavelength resolution (van der Kruk et al. 2015). Models with radial anisotropic constraints, i.e., SEMum-NA14, S362ANI and Krischer18, have better predictability of SH waves. Especially, model Crust1.0 predicts both the SH body waves and Love waves, possibly because of the the V_{sh} wave speed well constrained by both passive source data and active survey data.

It is noticeable that global models (S40RTS, S362ANI and GyPSuM) performs well in terms of predicting phase related observables (i.e., travel time and NZCC) in all three frequency ranges, even though they are not resolving small scale heterogeneities. It is reasonable because all those global models are constrained by mutiple datasets, including travel time, long-period body wave, and surface wave dispersion data. The body wave travel time, although based on ray-theory approximation and suffering from wavefront healing effect that reduces the amplitude of the wave speed anomaly thus lowers the resolution (Montelli et al. 2004), still predicts well the phase of seismic waves in short period range. The relatively evenly distributed earthquake and station locations in global model inversions may also help to balance the sensitive kernel of different geographical regions and different depths, which helps reduce the statistical bias of the model. This observation indicates that combining unbiased multiple measurements and data sets are critical for seismic wave speeds inversion. For a regional study, special attention should be paid to the possible unevenly distributed source and stations and a proper weighting scheme should be applied to mitigate the bias.

Since all models assessed are inverted from the phase (travel time, dispersion, etc.), it is reasonable that the absolute amplitude and L2 norm of the waveform misfits are not well

minimized yet, resulting in the unstable testing result for amplitude and waveform misfit comparison. Besides, the model attenuation also influences the absolute amplitude and waveforms, but is not yet constrained by any of the tested models. Sedimentary basins may produce strong reverberations which lead to complicated waveforms which are not predicted. Radial anisotropy is also not well constrained except for the two models S362ANI and SEMum-NA14. Therefore, a further model refinement for the contiguous US and surrounding regions aiming at short wavelength, small heterogeneity, and radial anisotropy in crustal and upper mantle is necessary. Since we still observe discrepancies of data and synthetic waveforms in long periods, it is important to start from long period waves to refine large-scale structures, and gradually add in higher frequency body and surface waves to better constrain small-scale heterogeneities in both the crust and mantle.

To conclude, in this realistic 3D mesh configuration of the contiguous US and surrounding regions, model S40RTS and S362ANI have the best overall performance in predicting both the body waves and long period surface waves, which may be benefited from high-quality and spatially balanced global measurements as well as multiple phases sensitive to both the upper and lower mantle structure. Model US.2016 best predicts the Rayleigh waves especially in the short period range. However, it performs less well than the S40RTS+Crust1.0 in predicting the SH waves which possibly due to the limited depth resolvability down to only 150 km depth and lack of the Love waves in their inversion data set. Models SEMum-NA14, GyPSuM and Krischer18 are also good at predicting long-period waveforms. Especially for model SEMum-NA14, it performs the best on predicting short epicentral distance SH and Love waves in 40-120 s, indicating the V_{sh} is well constrained in this model. For the crust, US.2016 does the best in predicting SV and Rayleigh waves while Crust1.0 performs better than US.2016 in predicting SH and Love waves, which suggest that the crust requires radial anisotropy to better predict the data on different components.

4.2 Initial Model Construction for FWIs

Although the waveform comparison and misfit measurements are able to present the waveform fitting of the tested models, the result does not necessarily indicate which model is better. Actually, it is difficult to evaluate the models because of the uncertainties in numerical modelling due to different model configurations between our test and the original inversion, including anisotropy, Q, topography, gravity, frequency range, and compatibility between the mantle and crust. Nevertheless, it is still meaningful to find out the compatibility of these models for a pre-designed realistic model configuration (including attenuation, topography, gravity, etc.)

that will be used for further FWI model refinements. A model with better data fitting shows higher compatibility and predictability, which makes it a good candidate for the initial model. However, more aspects apart from data-synthetics fitting need to be carefully considered to help constructing a better initial model for further FWIs.

The crustal model has significant influence on the data fitting. It is reported that for travel times measured in long periods, although mostly sensitive to mantle structure, are seconds different from the ray-theory prediction, which is related to the crustal effects (Ritsema et al. 2009). Therefore, in further FWI refinement, an accurate initial crust model, especially with detailed constraint of the shallow subsurface structure, is critical in precisely recover the wave speed structure of the deeper interior of the Earth. The compatibility of the crustal and mantle models is another important issue, reported by Bozdağ & Trampert (2008); Ritsema et al. (2009); Panning et al. (2010); Lekić & Romanowicz (2011) in terms of combining different crustal and mantle models. For example, model S40RTS shows a slightly better compatibility with Crust2.0 compared to Crust1.0 and crustal model from US.2016 (Fig. S11-S12 and Text S5) in terms of travel time misfit and NZCC. It is reasonable that model S40RTS uses Crust2.0 for the crustal correction (Ritsema et al. 2011). However, Crust1.0 is still more suitable for the initial model because it has more seismic constraints and better resolution than Crust2.0. Moreover, the crustal model from US.2016 combines short period Rayleigh wave and receiver functions which greatly improves the seismic constraints of the shallow subsurface SV wave speeds in contiguous US. The further FWI refinement will benefit from a better resolved crust.

Attenuation not only affects the absolute amplitude, but also causes phase shift which leads to travel time shift and waveform change. However in intermediate period ranges, the attenuation induced travel time shift is relatively small in terms of waveform (Tao et al. 2018) and statistics of misfits (Fig. S13-S14 and Text S6). In this paper and further FWI refinements, we use a hybrid Q model with $Q_\mu = 600$ in the crust and Q_μ from PREM model in the mantle. Nevertheless, the ultimate goal is to combine the measurement of absolute amplitude to invert for a better Q model with wave speeds model simultaneously using FWI (Zhu et al. 2013).

When selecting an initial model for FWI, the choice between 3D model with high-predictability and 1D reference model becomes debatable. 1D models does not bring in any prior wave speed anomaly patterns to the inversion, while a high resolution 3D model can provide more initial measurements when the FWI starts from intermediate periods. Our tests show that the initial model selection depends on the starting frequency range of the FWI. 1D reference models might not be a good choice if starting from intermediate period (20-40 s) since the initial misfit is high and the percentage of high CC measurement windows is limited. Implementing

a 3D crust on top of a 1D mantle model probably does not improve the initial data fitting. Our observations suggest the commonly used FWI starting model S362ANI is reasonable for not only the long but also the intermediate period ranges. The global 3D mantle model S40RTS also outperforms other models in our FWI configuration to invert seismic waves longer than 20 s period. Furthermore, the isotropic S40RTS model has the same level or even better data fitting as the radially anisotropic model S362ANI, which makes it an end-member initial model for further radially anisotropic FWIs because no prior radial anisotropy will be imprinted in the subsequent FWI.

Since there are fewer earthquake events in the central and eastern US, there will be very few short epicentral distance raypaths which senses the shallow subsurface in the crust. For a FWI work involving intermediate period waves, the surface waves are also less sensitive to the shallow subsurface structures. Therefore, it is important to get the crustal model, especially the shallow part, pre-constrained with an initial crustal model that can already predict the short-period surface waves and shallow-depth turning body waves. Regional models of the contiguous US such as US.2016 captures the local structures especially the shallow subsurface SV wave speeds, which makes US.2016 a good candidate model for the SV wave speed model of the crust. Crust1.0 better predicts SH waves than US.2016, which makes it a better candidate for the SH wave speed model in the crust.

Finally, a hybrid model combining surface-wave-tomography-constrained crust (i.e., US.2016) for V_{sv} and Crust1.0 for V_{sh}, and global model (i.e., S40RTS) for the mantle works better in terms of better initial waveform fitting (Fig. 12), which is suitable for further FWI model refinement.

5 CONCLUSION

By analyzing the travel time misfit, normalized zero-lag cross-correlation coefficient, and percentage of high waveform similarity measurement windows, we found that the compatible seismic models for the SPECFEM3D_GLOBE configuration of contiguous US and surrounding regions in the mantle are the global models (S40RTS and S362ANI); while in the crust are the surface wave derived model US.2016 (for V_{sv}) and active survey derived model CRUST1.0 (for V_{sh}). It is noticeable that tomographic models can best predict the long-period data used in their inversion. However, short period waves, i.e. 9-20 s, cannot be predicted by any of the tested models yet, due to the unaccounted radial anisotropy and small-scale heterogeneities in the shallow subsurface, for example, the sedimentary basins and crustal structures. Therefore, a further refinement of the wave speeds model of contiguous US and surrounding

regions is critical for better understanding the continental evolutions of the basin, crust, and mantle lithosphere. A hybrid initial model combining S40RTS or S362ANI in the mantle and US.2016 for V_{sv} and Crust1.0 for V_{sh} in the crust is optimal for future full waveform inversions to achieve higher resolution images of the crust and upper mantle structure.

ACKNOWLEDGMENTS

Models GyPSuM, SEMum-NA14, US-SL-2014, US.2016, S362ANI and AK135 are downloaded from the website of the Incorporated Research Institutions for Seismology (IRIS) Earth Model Collaboration (EMC) (http://ds.iris.edu/ds/products/emc/). Models S40RTS and Krischer18 are provided by Ritesma et al., (2011) and Krischer et al., (2018). Model CRUST1.0 is downloaded from the REM website (https://igppweb.ucsd.edu/ gabi/crust1.html). Seismic data are downloaded from the International Federation of Digital Seismograph Networks (FDSN, https://www.fdsn.org), Canadian National Seismic Network (CNSN, http://www.earthquakescanada.nrcan.gc.c and Servicio Sismológico Nacional (SSN, http://www.ssn.unam.mx). The earthquake CMT solutions are from the global CMT webpage (https://www.globalcmt.org). The open-source spectral-element software package SPECFEM3D_GLOBE and the moment-tensor inversion package CMT3D used for this article are freely available for download via the Computational Infrastructure for Geodynamics (CIG, https://geodynamics.org). Digital data of outlines of LIPS and hotspot locations are downloaded from http://www-udc.ig.utexas.edu/external/plates/data.htm. We thank Lion Krischer, Scott Burdick, and Incorporated Research Institutions for Seismology (IRIS) EMC for providing all the tomographic models. We also thank Lion Krischer, Andrew J. Schaeffer, Xyoli Pérez-Campos, and Robert Herrmann for their constructive discussion and suggestion regarding seismic model implementation or data acquisition. The seismic waveform data were downloaded from IRIS Data Management Center. We thank the Institute for Cyber-Enabled Research (ICER) at Michigan State University and the Extreme Science and Engineering Discovery Environment (XSEDE supported by NSF grant ACI-1053575) for providing the high-performance computing resources. This research was supported by NSF grant 1942431 and the startup fund of Min Chen at Michigan State University.

Table 1. Summary of the seismic models for validation

Models	Measurement	Dataset and frequency range	Model coverage
AK135	TT	Global stations before 1995	Global V_p, V_s, ρ
CRUST1.0	SF, RF, ACT	Global stations before 2013	Global layered crust V_p, V_s, ρ and Moho depth
GyPSuM	TT, GRA, GD	Global stations 1964-2007, 14-100 s	Global V_p, V_s and ρ, 0-2900 km
S40RTS	TT, SF, NM	Global stations before 2011	Global V_p, V_s, and ρ
US-SL-2014	TTR	USArray, NCEDC, SCEDC, 2011-2014, 1-20 s	$\delta \ln V_p$ and $\delta \ln V_s$, Contiguous US, 60-1220 km
SEMum-NA14	FWI, NM	USArray, North America stations before 2013, 40-120 s	V_{sv} and V_{sh}, 10-80N, 30-330W, 50-410 km
US.2016	ANT, SF, HV, RF	USArray stationss, 2006-2016, 8-90 s	V_s and Moho depth, Contiguous US, 0-150 km
Krischer18	FWI	FDSN hosted stations, 2005-2016, 30-120 s	V_p, V_{sv} and V_{sh}, 0-1440 km, North America and North Atlantic
S362ANI	TT, SF, WF	Global stations from 1994-2003, 50-200 s for WF and 35-150 s for SF	V_{sv} and V_{sh}, 25-2890 km, Global

Abbreviations for types of measurements: ACT: Active source survey; ANT: Ambient noise; FWI: full waveform inversion; GD: Geodetic measurements; GRA: Gravity measurements; HV: H/V ratio (Rayleigh wave ellipticity); NM: Normal mode; RF: Receiver function; SF: Surface wave dispersion; TT: Travel time; TTR: Travel-time residuals; WF: Waveform inversion using path average approximation.

Abbreviations for model velocities: V_s: shear wave speed; V_p: P-wave speed; V_{sh} horizontally traveling and horizontally polarized shear wave speed; V_{sv}: horizontally traveling and vertically polarized shear wave speed; Q: quality factor; ρ: density; δlnV: percentage perturbations relative to a 1D reference model.

Network abbreviations: NCEDC: Northern California Earthquake Data Center, SCEDC: Southern California Earthquake Data Center, FDSN: International Federation of Digital Seismograph Networks

Table 2. Empirical surface wave speed for window selection

Frequency range	Rayleigh wave speed	Love wave speed
9-20 s	3.2 km/s	3.7 km/s
20-40 s	3.3 km/s	3.9 km/s
40-120 s	3.5 km/s	4.2 km/s

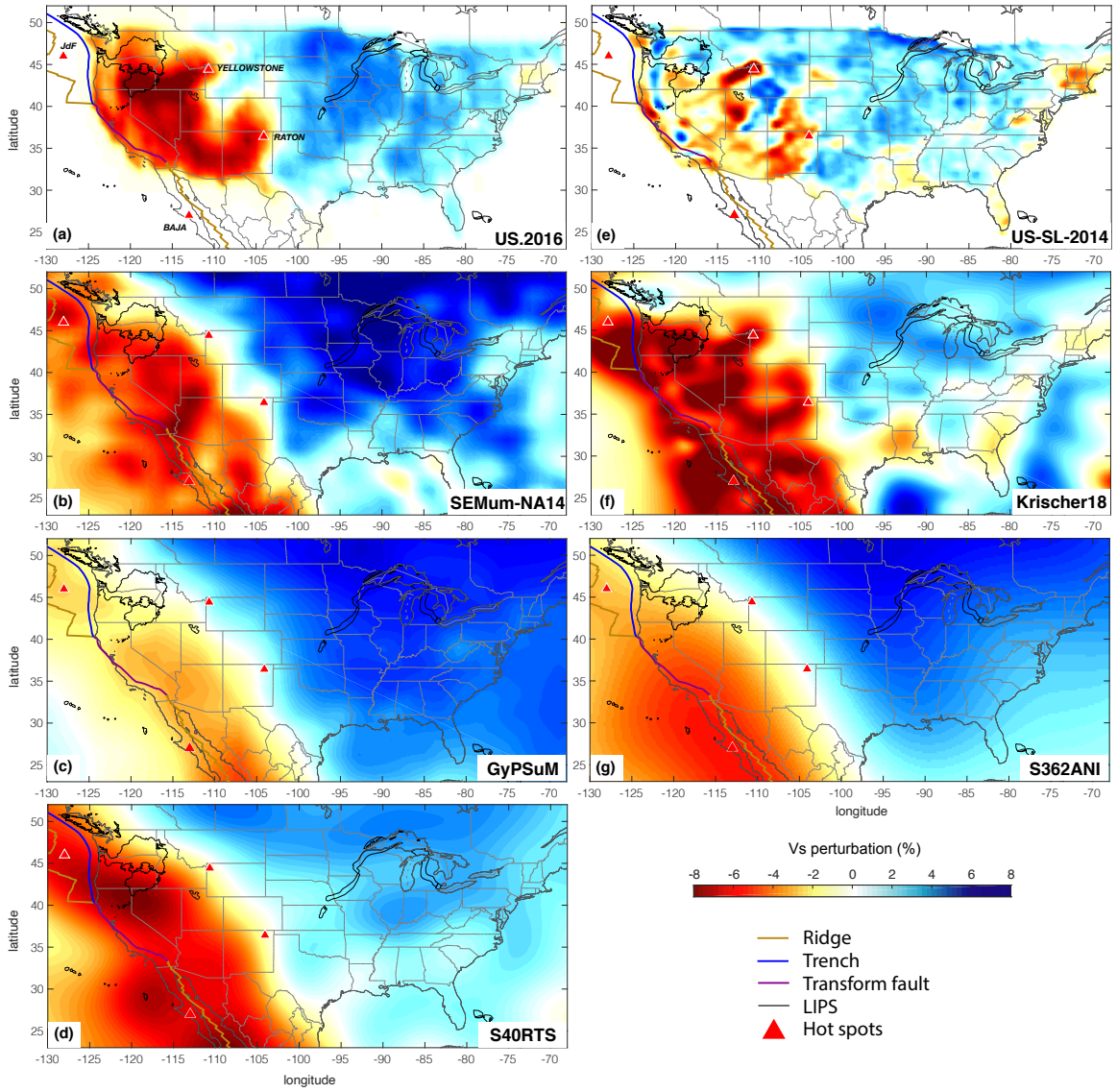

Figure 1. Comparison of seven shear wave speed models (US.2016, SEMum-NA14, GyPSuM, S40RTS, US-SL-2014, Krischer18 and S362ANI) beneath the contiguous US at 100 km depth. Shear wave perturbations are relative to 1D reference model AK135. For display purpose, all models are interpolated on even grids with a horizontal grid spacing of 0.25°. Models US.2016 and US-SL-2014 only cover part of the map region within the contiguous US and the rest of the map is filled with zero shear wave speed perturbation. Plate boundaries and large igneous provinces (LIPS) are marked with colored lines. Red triangles denote the hot spots or volcanic regions beneath Juan de Fuca plate, Yellowstone, Raton-Clayton and Baja California (Coffin et al. 2005).

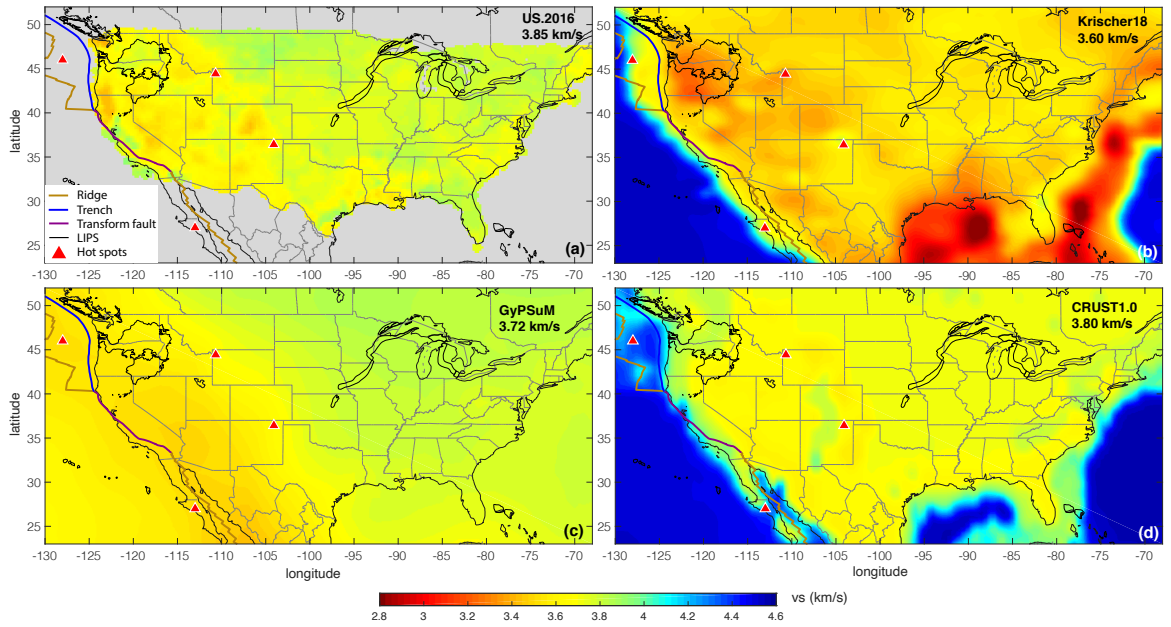

Figure 2. Maps of absolute shear wave speeds of the four selected crustal models at 20 km depth. (a) model US.2016; (b) model Krischer18; (c) model GyPSuM; (d) model CRUST1.0. Only models US.2016, Krischer18 and GyPSuM have crustal structure provided, all the other tested models are implemented with model CRUST1.0 in the crust. Model US.2016 only covers part of the map region and the rest is filled up with gray color (in the mesh implementation, Crust1.0). The marked geological units are the same as those in Figure 1.

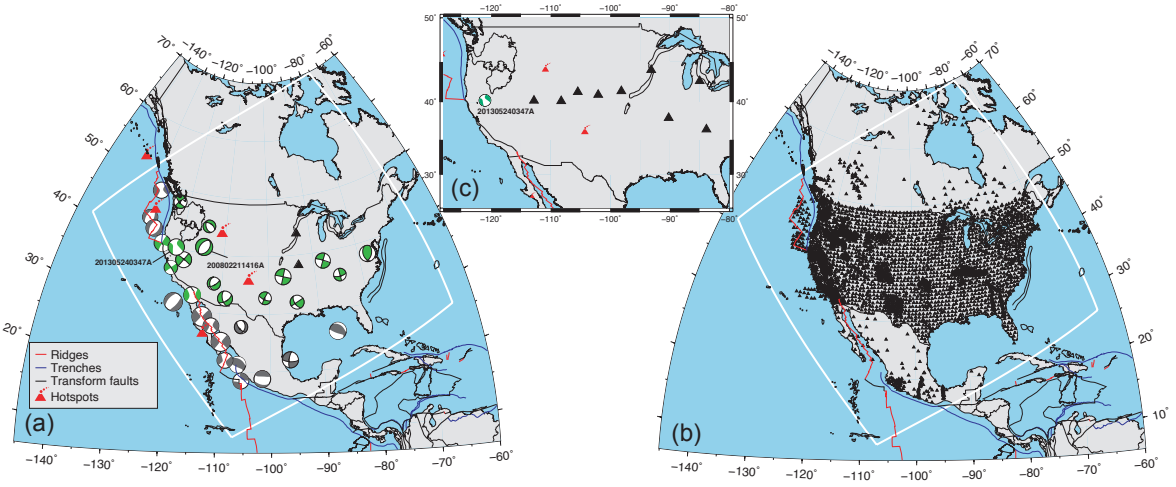

Figure 3. Event and station distribution in the simulation region. 30 events (a) and all stations (b) are used for waveform misfit comparison amongst different test models. Green colored beachballs are contiguous US events, while dark gray colored beachballs are other events outside contiguous US. White box outlines the simulation region. (c) The earthquake 201305240347A (Mw 5.7) for waveform comparison examples, and the stations along an approximate E-W profile with event back azimuth within 10 degrees of deviation.

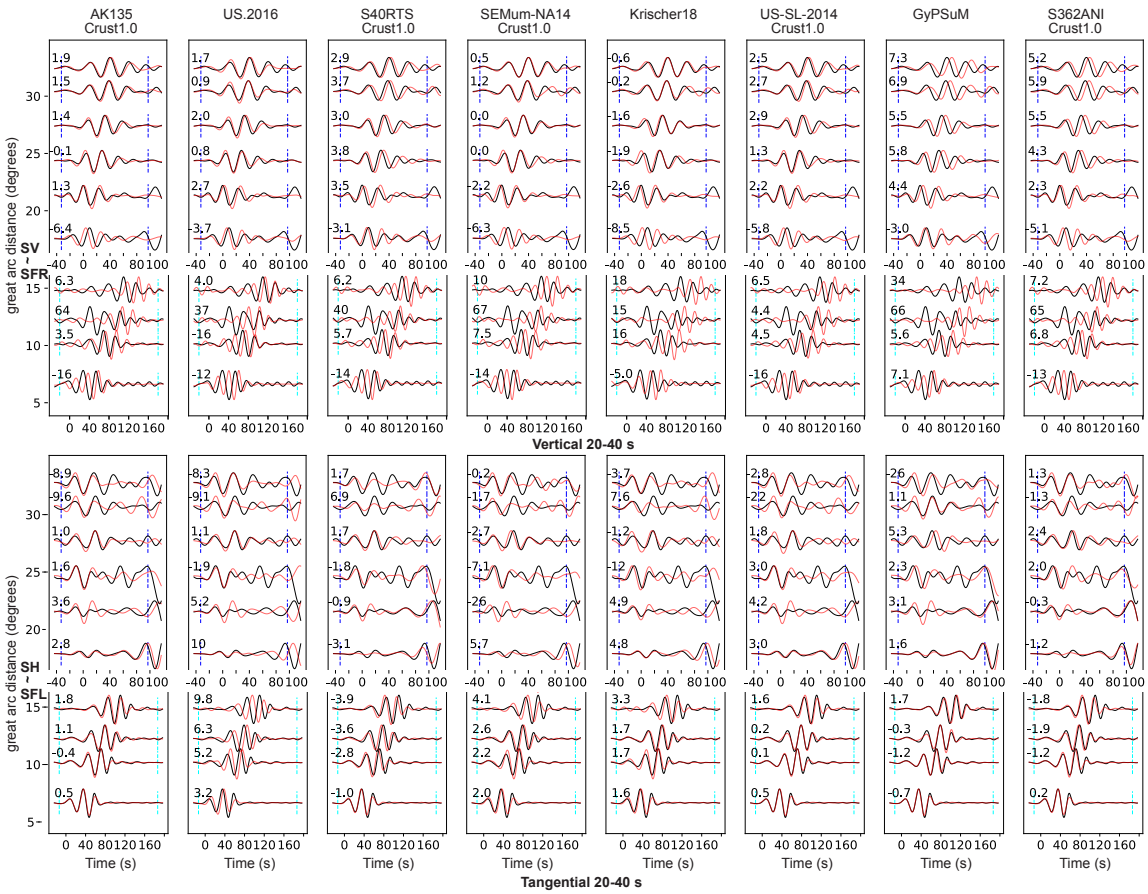

Figure 4. Waveform comparison for intermediate period shear wave (20-40 s) on vertical and tangential components. Traces are shown in Fig. 3, aligned with reduced time reference to the S-wave arrival time predicted by AK135. Black and red lines are the observed and synthetic waveforms, respectively. For local traces, surface wave takes over S wave phases. Blue and cyan dashed lines mark the shear wave and surface wave measurement windows, respectively. Numbers mark the cross-correlation measured travel time difference between synthetics and data.

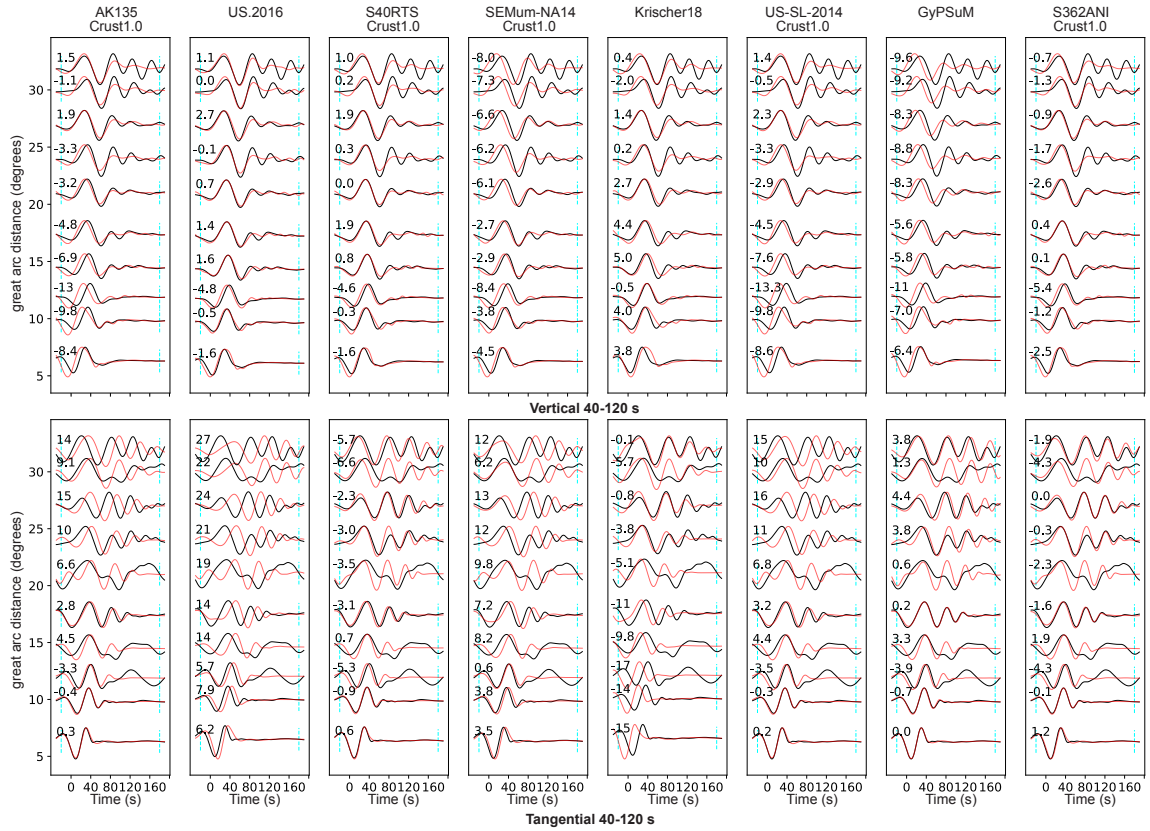

Figure 5. Waveform comparison for long period surface wave (40-120 s) on vertical and tangential components. Traces are shown in Fig. 3, aligned with the empirical arrival time of Rayleigh or Love waves calculated by empirical surface wave speeds in Table. 2. Cyan dashed lines mark the surface wave measurement windows. Numbers mark the cross-correlation measured travel time difference between synthetics and data.

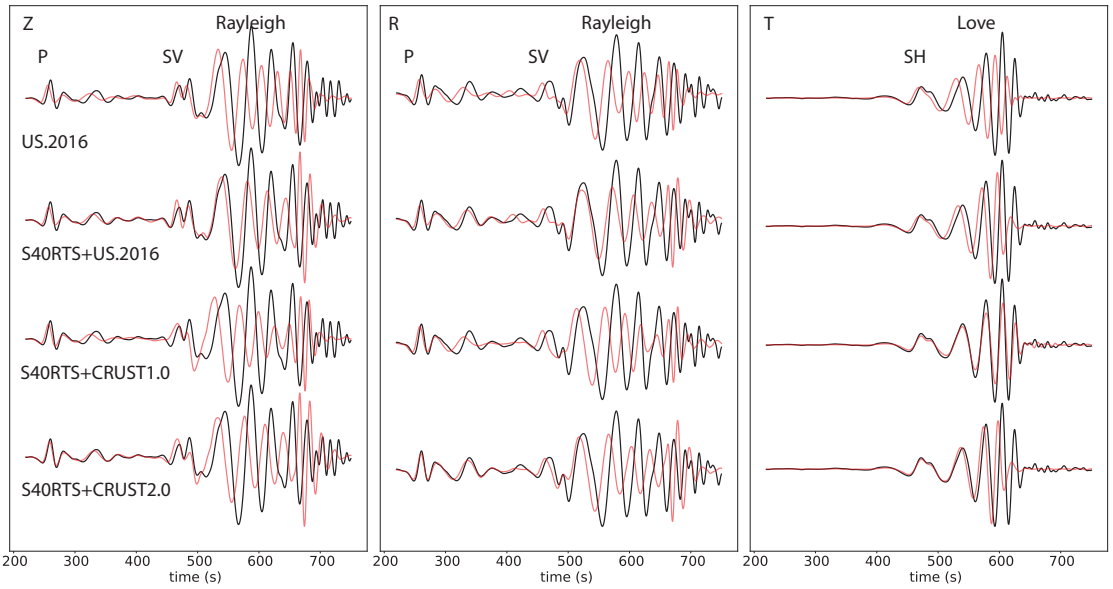

Figure 6. Waveform comparison of the same mantle model S40RTS with different crustal models. Event: 200802211416A (Mw 6.0); station: IU.CCM. Epicentral distance: 17.9°. Red and black lines are synthetic and observation waveforms, respectively.

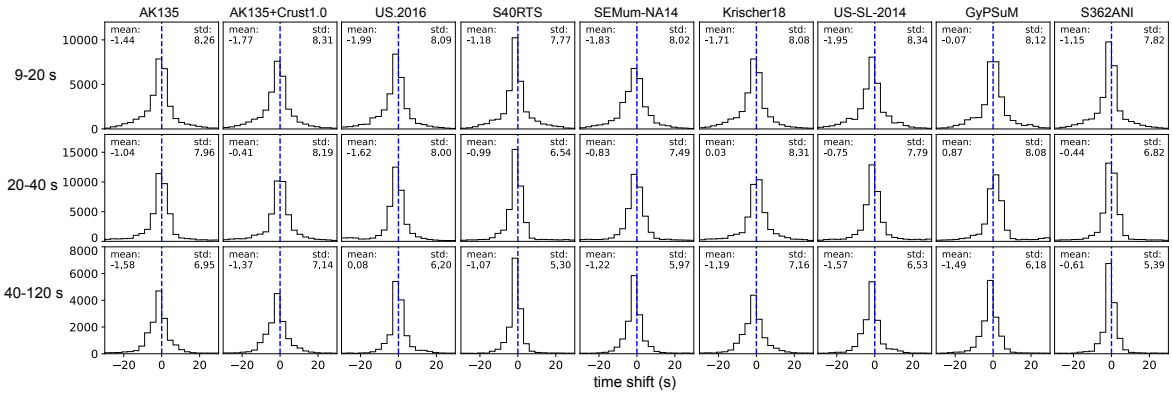

Figure 7. Travel time shift distribution histograms for all the measurement windows. Rows upper to lower: 9-20 s, 20-40 s and 40-120 s; Panels left to right: different models.

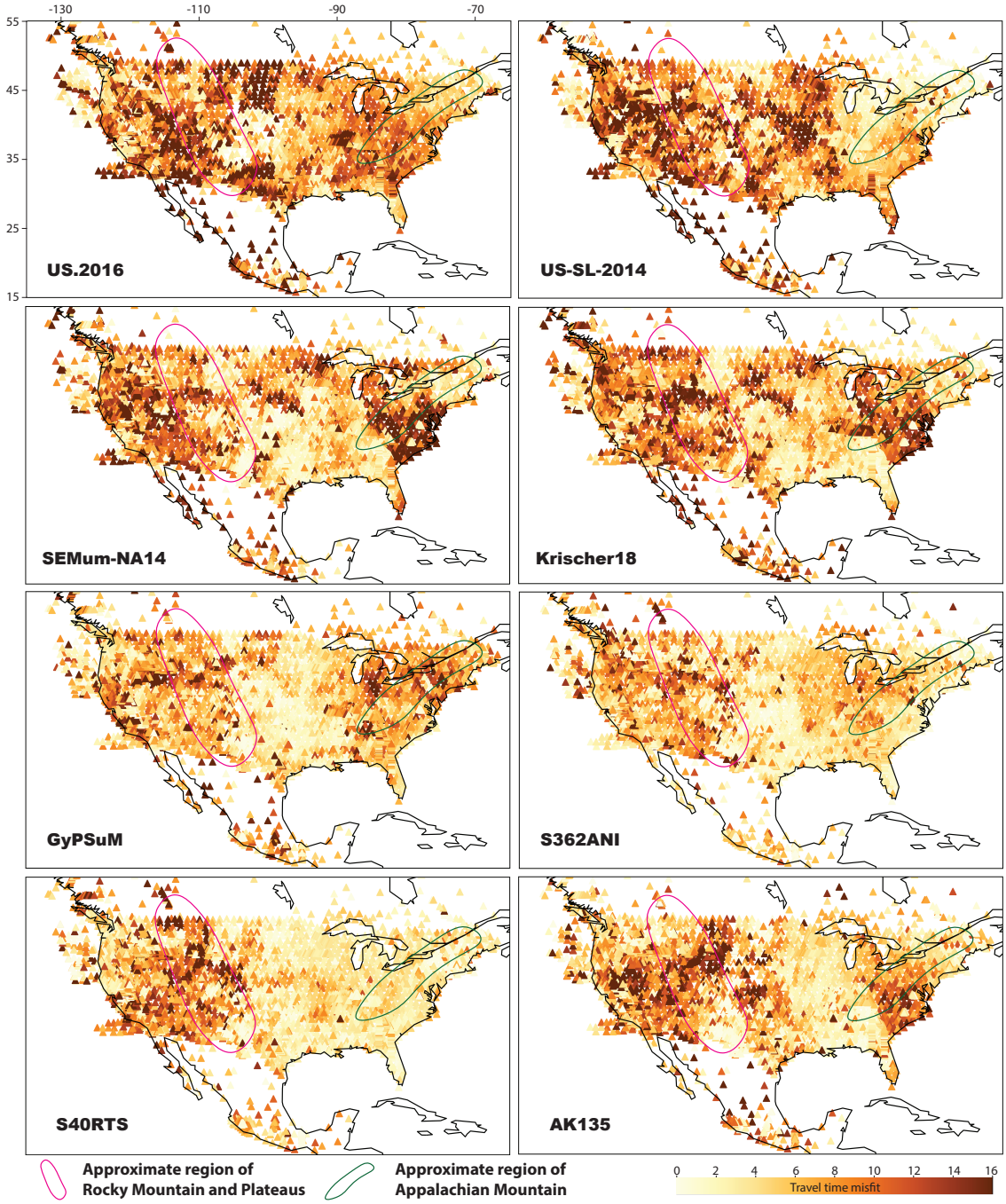

Figure 8. Averaged shear wave travel time misfit at each station for all the testing events. Stations are color coded by travel time misfit value in 20-40 s. Each panel are different models.

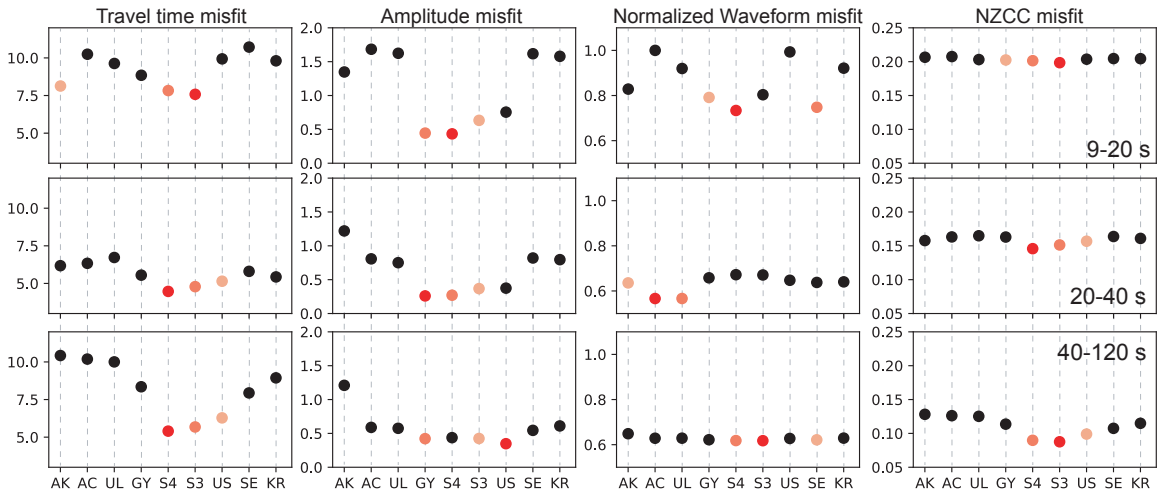

Figure 9. Four types of misfit for contiguous US events in three period ranges. Rows upper to lower: 9-20 s, 20-40 s and 40-120 s; Panels left to right: travel time, amplitude, waveform and zerolag CC misfits, respectively. First 3 models with minimum misfits are marked with different reds. The x-axis marks are for different models: AK: AK135, AC: AK135+Crust1.0, UL: US-SL-2014, GY: GyPSuM, S4: S40RTS, S3: S362ANI, US: US.2016, SE: SEMum-NA14, KR: Krischer18. Models UL, S4, S3 and SE are implemented with Crust1.0 on top.

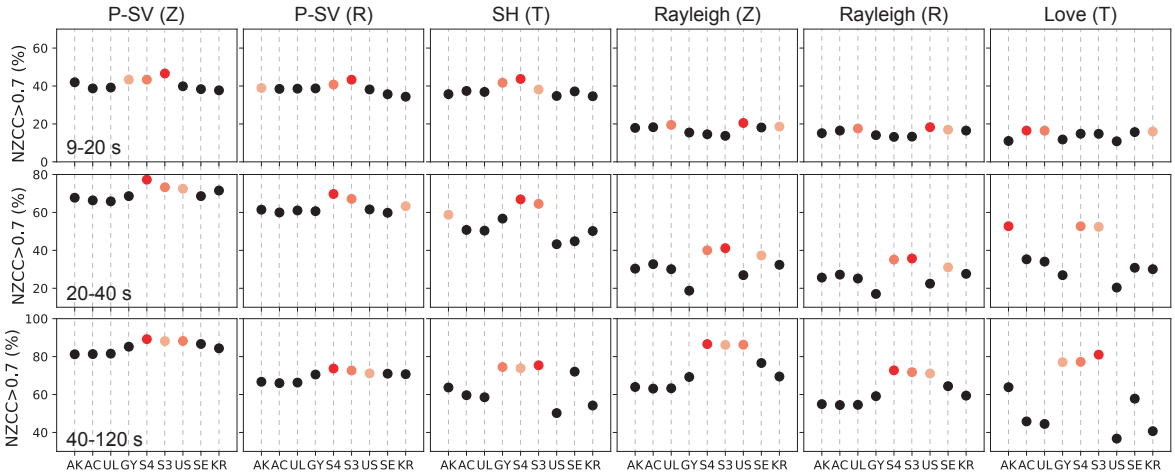

Figure 10. Model predictability defined by the percentage of NZCC>0.7. Rows upper to lower: 9-20 s, 20-40 s and 40-120 s; Panels left to right: 6 categories (P-SV Z, P-SV R, SH T, Rayleigh Z, Rayleigh R and Love T). First 3 models with maximum percentage of NZCC>0.7 measurements are marked with different reds. The x-axis marks are for different models: AK: AK135, AC: AK135+Crust1.0, UL: US-SL-2014, GY: GyPSuM, S4: S40RTS, S3: S362ANI, US: US.2016, SE: SEMum-NA14, KR: Krischer18. Models UL, S4, S3 and SE are implemented with Crust1.0 on top.

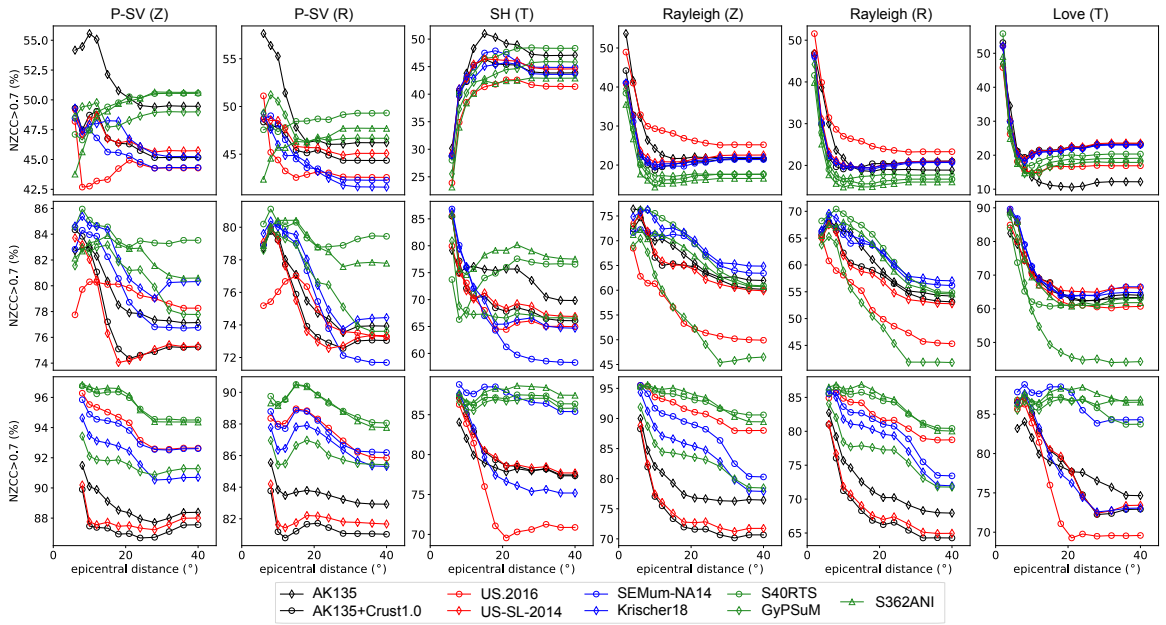

Figure 11. Model predictability vs. different epicentral distances. The percentage of measurements with NZCC>0.7 within certain epicentral distances are plotted for different seismic phases in 6 categories (columns left to right: P-SV Z, P-SV R, SH T, Rayleigh Z, Rayleigh R and Love T) in different period ranges (rows top to bottom, 9–20 s, 20–40 s, and 40–120 s). Higher percentages indicate better model predictability.

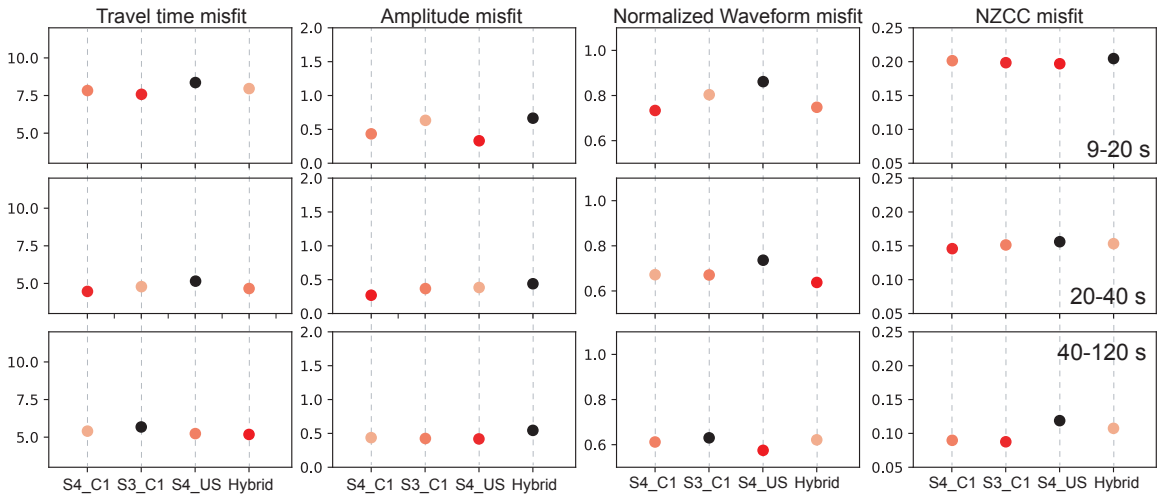

Figure 12. Four types of misfit for contiguous US events in three period ranges. Rows upper to lower: 9-20 s, 20-40 s and 40-120 s; Panels left to right: travel time, amplitude, waveform and zerolag CC misfits, respectively. First 3 models with minimum misfits are marked with different reds. The x-axis marks are for different models: S4_C1: S40RTS mantle with Crust1.0; S3_C1: S362ANI mantle with Crust1.0; S4_US: S40RTS mantle with US.2016 crust; Hybrid: hybrid model with S40RTS mantle, US.2016 crust for SV and Crust1.0 for SH.

REFERENCES

Alex Song, T.-R. & Helmberger, D. V., 2007. Validating tomographic model with broad-band waveform modelling: an example from the la ristra transect in the southwestern united states, *Geophysical Journal International*, **171**(1), 244–258.

Bao, X. & Shen, Y., 2016. Assessing waveform predictions of recent three-dimensional velocity models of the Tibetan Plateau, *Journal of Geophysical Research: Solid Earth*, **121**, 2521–2538.

Bedle, H. & van der Lee, S., 2009. S velocity variations beneath north america, *Journal of Geophysical Research: Solid Earth*, **114**(B7).

Bozdağ, E. & Trampert, J., 2008. On crustal corrections in surface wave tomography, *Geophysical Journal International*, **172**(3), 1066–1082.

Bozdağ, E. & Trampert, J., 2010. Assessment of tomographic mantle models using spectral element seismograms, *Geophysical Journal International*, **180**(3), 1187–1199.

Bozdağ, E., Peter, D., Lefebvre, M., Komatitsch, D., Tromp, J., Hill, J., Podhorszki, N., & Pugmire, D., 2016. Global adjoint tomography: first-generation model, *Geophysical Journal International*, **207**(3), 1739–1766.

Buehler, J. & Shearer, P., 2017. Uppermost mantle seismic velocity structure beneath usarray, *Journal of Geophysical Research: Solid Earth*, **122**(1), 436–448.

Burdick, S., Vernon, F. L., Martynov, V., Eakins, J., Cox, T., Tytell, J., Mulder, T., White, M. C., Astiz, L., Pavlis, G. L., et al., 2017. Model update may 2016: Upper-mantle heterogeneity beneath north america from travel-time tomography with global and usarray data, *Seismological Research Letters*, **88**(2A), 319–325.

Chen, M., Niu, F., Liu, Q., & Tromp, J., 2015a. Mantle-driven uplift of hangai dome: New seismic constraints from adjoint tomography, *Geophysical Research Letters*, **42**(17), 6967–6974.

Chen, M., Niu, F., Liu, Q., Tromp, J., & Zheng, X., 2015b. Multiparameter adjoint tomography of the crust and upper mantle beneath east asia: 1. model construction and comparisons, *Journal of Geophysical Research: Solid Earth*, **120**(3), 1762–1786.

Chen, M., Niu, F., Tromp, J., Lenardic, A., Lee, C.-T. A., Cao, W., & Ribeiro, J., 2017. Lithospheric foundering and underthrusting imaged beneath tibet, *Nature communications*, **8**, 15659.

Chen, M., Manea, V. C., Niu, F., Wei, S. S., & Kiser, E., 2019. Genesis of intermediate-depth and deep intraslab earthquakes beneath japan constrained by seismic tomography, seismicity, and thermal modeling, *Geophysical Research Letters*, **46**(4), 2025–2036.

Coffin, M. F., Eldholm, O., et al., 2005. Large igneous provinces, *Encyclopedia of Geology*, pp. 315–323.

Coleman Jr, J. L. & Cahan, S. M., 2012. Preliminary catalog of the sedimentary basins of the united states.

Ekström, G., Nettles, M., & Dziewoński, A., 2012. The global cmt project 2004–2010: Centroid-moment tensors for 13,017 earthquakes, *Physics of the Earth and Planetary Interiors*, **200**, 1–9.

Engdahl, E. R., van der Hilst, R., & Buland, R., 1998. Global teleseismic earthquake relocation with improved travel times and procedures for depth determination, *Bulletin of the Seismological Society of America*, **88**(3), 722–743.

Ferreira, A., Woodhouse, J., Visser, K., & Trampert, J., 2010. On the robustness of global radially anisotropic surface wave tomography, *Journal of Geophysical Research: Solid Earth*, **115**(B4).

Fichtner, A., Kennett, B. L., Igel, H., & Bunge, H.-P., 2009. Full seismic waveform tomography for upper-mantle structure in the australasian region using adjoint methods, *Geophysical Journal International*, **179**(3), 1703–1725.

Fichtner, A., Kennett, B. L., Igel, H., & Bunge, H.-P., 2010. Full waveform tomography for radially anisotropic structure: new insights into present and past states of the australasian upper mantle, *Earth and Planetary Science Letters*, **290**(3-4), 270–280.

Gao, H. & Shen, Y., 2012. Validation of shear-wave velocity models of the pacific northwest, *Bulletin of the Seismological Society of America*, **102**(6), 2611–2621.

Gao, H. & Shen, Y., 2015. Validation of recent shear wave velocity models in the united states with full-wave simulation, *Journal of Geophysical Research: Solid Earth*, **120**(1), 344–358.

Jia, Z., Ni, S., Chu, R., & Zhan, Z., 2017. Joint inversion for earthquake depths using local waveforms and amplitude spectra of rayleigh waves, *Pure and Applied Geophysics*, **174**(1), 261–277.

Jiang, C., Schmandt, B., Hansen, S. M., Dougherty, S. L., Clayton, R. W., Farrell, J., & Lin, F.-C., 2018. Rayleigh and s wave tomography constraints on subduction termination and lithospheric foundering in central california, *Earth and Planetary Science Letters*, **488**, 14–26.

Kennett, B. L., Engdahl, E., & Buland, R., 1995. Constraints on seismic velocities in the earth from traveltimes, *Geophysical Journal International*, **122**(1), 108–124.

Komatitsch, D. & Tromp, J., 2002a. Spectral-element simulations of global seismic wave propagation—i. validation, *Geophysical Journal International*, **149**(2), 390–412.

Komatitsch, D. & Tromp, J., 2002b. Spectral-element simulations of global seismic wave propagation—ii. three-dimensional models, oceans, rotation and self-gravitation, *Geophysical Journal International*, **150**(1), 303–318.

Komatitsch, D., Vilotte, J.-P., Tromp, J., Afanasiev, M., Bozdag, E., Charles, J., Chen, M., Goddeke, D., Hjorleifsdottir, V., Labarta, J., Le Goff, N., Le Loher, P., Liu, Q., Maggi, A., Martin, R., McRitchie, D., Messmer, P., Michea, D., Nissen-Meyer, T., Peter, D., Rietmann, M., de Andrade, S., Savage, B., Schuberth, B., Siemenski, A., Strand, L., Tape, C., Xie, Z., & Zhu, H., 9999. Specfem3d globe [software].

Krischer, L., Fichtner, A., Boehm, C., & Igel, H., 2018. Automated large-scale full seismic waveform inversion for north america and the north atlantic, *Journal of Geophysical Research: Solid Earth*, **123**(7), 5902–5928.

Kustowski, B., Ekström, G., & Dziewoński, A., 2008. Anisotropic shear-wave velocity structure of the earth's mantle: A global model, *Journal of Geophysical Research: Solid Earth*, **113**(B6).

Laske, G., Masters, G., Ma, Z., & Pasyanos, M., 2013. Update on crust1. 0—a 1-degree global model of earth's crust, in *Geophys. Res. Abstr*, vol. 15, p. 2658, EGU General Assembly Vienna, Austria.

Lee, E.-J., Chen, P., & Jordan, T. H., 2014. Testing waveform predictions of 3D velocity models against two recent Los Angeles earthquakes, *Seismological Research Letters*, **85**(6), 1275–1284.

Lekić, V. & Romanowicz, B., 2011. Inferring upper-mantle structure by full waveform tomography with the spectral element method, *Geophysical Journal International*, **185**(2), 799–831.

Lin, F.-C., Schmandt, B., & Tsai, V. C., 2012. Joint inversion of rayleigh wave phase velocity and ellipticity using usarray: Constraining velocity and density structure in the upper crust, *Geophysical Research Letters*, **39**(12).

Lin, F.-C., Tsai, V. C., & Schmandt, B., 2014. 3-d crustal structure of the western united states: application of rayleigh-wave ellipticity extracted from noise cross-correlations, *Geophysical Journal International*, **198**(2), 656–670.

Lin, Y.-P., Zhao, L., & Hung, S.-H., 2011. Assessment of tomography models of Taiwan using first-arrival times from the TAIGER active-source experiment, *Bulletin of the Seismological Society of America*, **101**(2), 866–880.

Liu, Q., Polet, J., Komatitsch, D., & Tromp, J., 2004. Spectral-element moment tensor inversions for earthquakes in southern california, *Bulletin of the Seismological Society of America*, **94**(5), 1748–1761.

Liu, Y., Teng, J., Xu, T., Wang, Y., Liu, Q., & Badal, J., 2016. Robust time-domain full waveform inversion with normalized zero-lag cross-correlation objective function, *Geophysical Journal International*, **209**(1), 106–122.

Maceira, M., Larmat, C., Porritt, R. W., Higdon, D. M., Rowe, C. A., & Allen, R. M., 2015. On the validation of seismic imaging methods: Finite frequency or ray theory?, *Geophysical Research Letters*, **42**, 323–330.

Montelli, R., Nolet, G., Masters, G., Dahlen, F., & Hung, S.-H., 2004. Global p and pp traveltime tomography: rays versus waves, *Geophysical Journal International*, **158**(2), 637–654.

Mulder, W. & Plessix, R.-E., 2008. Exploring some issues in acoustic full waveform inversion, *Geophysical Prospecting*, **56**(6), 827–841.

Nelson, P. L. & Grand, S. P., 2018. Lower-mantle plume beneath the yellowstone hotspot revealed by core waves, *Nature Geoscience*, **11**(4), 280.

Panning, M., Lekić, V., & Romanowicz, B., 2010. Importance of crustal corrections in the development of a new global model of radial anisotropy, *Journal of Geophysical Research: Solid Earth*, **115**(B12).

Pavlis, G. L., Sigloch, K., Burdick, S., Fouch, M. J., & Vernon, F. L., 2012. Unraveling the geometry of the farallon plate: Synthesis of three-dimensional imaging results from usarray, *Tectonophysics*, **532**, 82–102.

Porritt, R. W., Allen, R. M., & Pollitz, F. F., 2014. Seismic imaging east of the rocky mountains with usarray, *Earth and Planetary Science Letters*, **402**, 16–25.

Qin, Y., Capdeville, Y., Montagner, J.-P., Boschi, L., & Becker, T. W., 2009. Reliability of mantle tomography models assessed by spectral element simulation, *Geophysical Journal International*, **177**(1), 125–144.

Ritsema, J., Van Heijst, H., Woodhouse, J., & Deuss, A., 2009. Long-period body wave traveltimes through the crust: implication for crustal corrections and seismic tomography, *Geophysical Journal International*, **179**(2), 1255–1261.

Ritsema, J., Deuss, a. A., Van Heijst, H., & Woodhouse, J., 2011. S40rts: a degree-40 shear-velocity model for the mantle from new rayleigh wave dispersion, teleseismic traveltime and normal-mode splitting function measurements, *Geophysical Journal International*, **184**(3), 1223–1236.

Robertsson, J. O., 1996. A numerical free-surface condition for elastic/viscoelastic finite-difference modeling in the presence of topography, *Geophysics*, **61**(6), 1921–1934.

Ruan, Y., Lei, W., Modrak, R., Örsvuran, R., Bozdağ, E., & Tromp, J., 2019. Balancing unevenly distributed data in seismic tomography: a global adjoint tomography example, *Geophysical Journal International*, **219**(2), 1225–1236.

Schmandt, B. & Humphreys, E., 2010. Complex subduction and small-scale convection revealed by body-wave tomography of the western united states upper mantle, *Earth and Planetary Science Letters*, **297**(3-4), 435–445.

Schmandt, B. & Lin, F.-C., 2014. P and s wave tomography of the mantle beneath the united states, *Geophysical Research Letters*, **41**(18), 6342–6349.

Schmandt, B., Lin, F.-C., & Karlstrom, K. E., 2015. Distinct crustal isostasy trends east and west of the rocky mountain front, *Geophysical Research Letters*, **42**(23), 10–290.

Shen, W. & Ritzwoller, M. H., 2016. Crustal and uppermost mantle structure beneath the united states, *Journal of Geophysical Research: Solid Earth*, **121**(6), 4306–4342.

Simmons, N. A., Forte, A. M., Boschi, L., & Grand, S. P., 2010. Gypsum: A joint tomographic model of mantle density and seismic wave speeds, *Journal of Geophysical Research: Solid Earth*, **115**(B12).

Taborda, R., Azizzadeh-Roodpish, S., Khoshnevis, N., & Cheng, K., 2016. Evaluation of the southern California seismic velocity models through simulation of recorded events, *Geophysical Journal International*, **205**, 1342–1364.

Tao, K., Grand, S. P., & Niu, F., 2017. Full-waveform inversion of triplicated data using a normalized-correlation-coefficient-based misfit function, *Geophysical Journal International*, **210**(3), 1517–1524.

Tao, K., Grand, S. P., & Niu, F., 2018. Seismic structure of the upper mantle beneath eastern asia from full waveform seismic tomography, *Geochemistry, Geophysics, Geosystems*, **19**(8), 2732–2763.

Tape, C., Liu, Q., Maggi, A., & Tromp, J., 2010. Seismic tomography of the southern california crust based on spectral-element and adjoint methods, *Geophysical Journal International*, **180**(1), 433–462.

Tromp, J., Tape, C., & Liu, Q., 2005. Seismic tomography, adjoint methods, time reversal and banana-doughnut kernels, *Geophysical Journal International*, **160**(1), 195–216.

van der Kruk, J., Gueting, N., Klotzsche, A., He, G., Rudolph, S., von Hebel, C., Yang, X., WeihermŘller, L., Mester, A., & Vereecken, H., 2015. Quantitative multi-layer electromagnetic induction inversion and full-waveform inversion of crosshole ground penetrating radar data, *Journal of Earth Science*, **26**(6), 844–850.

Yuan, H., French, S., Cupillard, P., & Romanowicz, B., 2014. Lithospheric expression of geological units in central and eastern north america from full waveform tomography, *Earth and Planetary Science Letters*, **402**, 176–186.

Zhou, T., Meng, L., Xie, Y., & Han, J., 2019. An adjoint-state full-waveform tsunami source inversion method and its application to the 2014 chile-iquique tsunami event, *Journal of Geophysical Research: Solid Earth*, **124**(7), 6737–6750.

Zhu, H., Bozdağ, E., Duffy, T. S., & Tromp, J., 2013. Seismic attenuation beneath europe and the north atlantic: Implications for water in the mantle, *Earth and Planetary Science Letters*, **381**, 1–11.

Zhu, H., Komatitsch, D., & Tromp, J., 2017. Radial anisotropy of the north american upper mantle based on adjoint tomography with usarray, *Geophysical Journal International*, **211**(1), 349–377.

submitted to *Geophys. J. Int.*

Supplementary material for "Initial model construction for intermediate-period full-waveform inversion of the contiguous U.S. and surrounding regions"

Tong Zhou, Ziyi Xi, Min Chen and Jiaqi Li

SUMMARY This supplementary material contains 6 texts and 13 figures.

Text S1 Model implementation in detail

(1) S40RTS and S362ANI: Mostly the original implementation in SPECFEM3D_GLOBE, but switch the crustal model to Crust1.0.

(2) GyPSuM: First convert the absolute velocity to perturbations of the reference model AK135, and then implement in the mesh. No crust1.0 is attached because GyPSuM is starting at 0 km. The wave speed is stretched according to the topography.

(3) US.2016: The model contains Vs and assigned Vp in 0-150 km within contiguous U.S region and Moho depth. The Moho depth is implemented. 0-Moho: assign ρ according to Crust1.0, stretch the wave speed according to the Moho depth and topography. Moho-150: assign ρ according to AK135. Below 150: Attach model AK135. Outside contiguous U.S: above Moho attach Crust1.0 and below Moho attach AK135. The Moho depth, crustal model and mantle model are smoothed with a Gaussian filter with a radius of 1.25° horizontally and 10 km in the mantle and 2 km in the crust vertically to avoid any artificial discontinuities.

(4) US-SL-2014: The model contains Vp and Vs in 60-1220 km within contiguous U.S region. We use Crust1.0 for crust and Moho. The wave speed in the crust is stretched according to the Moho depth and topography, and the wave speed of the mantle is stretched to fit gap between the Moho and 60 km. Below 1220: attach model AK135. Outside contiguous U.S: above Moho attach Crust1.0 and below Moho attach AK135. The model are smoothed with

a Gaussian filter with a radius of 1.25° horizontally and 10 km in the mantle and 2 km in the crust vertically to avoid any artificial discontinuities.

(5) SEMum-NA14: The model contains Vsv and Vsh from 50-410 km in the whole North America region. We use Crust1.0 for crust and Moho. The wave speed in the crust is stretched according to the Moho depth and topography, and the wave speed of the mantle is stretched to fit gap between the Moho and 50 km. Vp is assigned using a constant Vp/Vs ratio of 1.73. Below 1220: attach model AK135. The model are smoothed with a Gaussian filter with a radius of 1.25° horizontally and 10 km in the mantle and 2 km in the crust vertically to avoid any artificial discontinuities.

(6) Krischer18: The model contains Vp, Vsv and Vsh from 0-1440 km in the whole North America region. No Moho depth is provided. We implement the Moho from Crust1.0 and implement the model wave speeds only. Below 1440: attach AK135.

All the models represented by wave speed perturbations are converted to the absolute wave speeds using the 1-D reference model provided by each tomographic study.

Text S2 Earthquake source parameters re-inversion. The global CMT source solutions (Ekström et al. 2012) applies 40 s W-phase to constrain the event location and moment tensor, which may not accurate in short period ranges and does not account for the 3-D structural effects. We re-invert for the source parameters using a 3-D crustal model CRUST1.0 embedded in 1-D AK135 reference mantle model in order to mitigate measurement bias due to the source re-inversion. We apply a hybrid approach. First, a grid search method is used to find the optimal event depth that minimizes both the cut-and-paste waveform similarity (similar as Zhu & Helmberger (1996)) and Rayleigh wave spectrum (Jia et al. 2017). The Love wave spectrum is observed to be not sensitive to the depth change of the earthquake source. The measurements at each station are divided into 16 azimuthal bins to apply azimuthal weighting. The objective function for grid search in each azimuthal bin is expressed as:

$$E^b(h) = E_c^b(h) + E_s^b(h) = \sum_1^n \left(\frac{r}{r_0}\right)^p \sqrt{\sum_t [u_i - s_i(h)]^2} + \sum_{i=1}^n \sum_{k=1}^W \frac{1}{W} \left| \log_{10} \left(\frac{\mathrm{A_{obs}}(\omega_\mathrm{k}, \mathrm{h}, \mathrm{i})}{\mathrm{A_{syn}}(\omega_\mathrm{k}, \mathrm{h}, \mathrm{i})} \right) \right| \quad (1)$$

where $E_c^b(h)$ is the waveform misfit in the b-th azimuthal bin after the data and synthetics are aligned for all seismic phases considered including P, S , Rayleigh and Love waves; $E_s^b(h)$, the Rayleigh wave spectrum misfit in the b-th azimuthal bin; $(r/r_0)^p$, a distance-based weight that compensates the geometry spreading; u_i is the observed waveform at the i-th station; $s_i(h)$, the synthetic waveform calculated with source depth of h; W, the number of sampled frequencies; $A_{obs}(\omega_k h, i)$ and $A_s yn(\omega_k h, i)$, the amplitude spectra of the observed and the

synthetic Rayleigh waves respectively. This combined misfit function is very sensitive to the source depth changes. The overall misfit function is calculated by summing the misfit in different azimuthal bins weighted by the station density in each bin. Subsequently, a linear source inversion algorithm, CMT3D (Liu et al. 2004), is performed to re-invert the moment tensors using the 3-D Green's functions. Fig. S1 shows an example of the event relocation result of the 200802211416A earthquake event. The re-inversion improves the waveform fitting for US.2016 for local and regional waveforms in the period ranges of 10–40 s and 15–80 s on the vertical and radial components. However, there is no noticeable improvement in the waveform fitting on the tangential components, possibly due to the V_sh wave speeds are less accurate in the crust and need further improvements.

Text S3 Short-period (9-20 s) waveform comparison along the measuring profile (Fig. S2). The shear wave fitting is generally low for all the models, especially the tangential component (Fig. S3). Among the models, S40RTS and US-SL-2014 are relatively better at predicting the shear wave on vertical and radial components at larger epicentral distances ($20^\circ - 30^\circ$), followed by model US.2016. The very low shear wave amplitudes within $10^\circ - 15^\circ$ related to the nodal plane are not well predicted by any of the models due to the possibly inaccurate source parameters. Surface waves in period range of 9-20 s are most sensitive to the crustal structure. Therefore, we show the waveform fitting for different crustal models in Fig. S4. Low surface waveform fitting for all the models in 9-20 s are observed. The observation is complicated with strong coda reverberations, which may related to reverberations triggered by the deep sedimentary basins (e.g., Forest City, Cherokee and Illinois (Coleman Jr & Cahan 2012), Fig. S2). Currently, none of the models can predict the waveform complexities in around 10 s period due to the complexity of basin structures as well as the compatibility of topography and model interpolations, which needs further refinement.

Text S4 We analyze the variation of travel time shift distributions for body wave and surface wave separately. In the body wave travel time shift distribution histogram (Fig. S5), it seems that for short period range (9-20 s) and long period range (40-120 s), every model has similar standard deviation. In 20-40 s intermediate period range, models S40RTS and S362ANI has significant lower standard deviation than other models. There is still systematic negative mean for almost every model in every period ranges. For the surface wave travel time shift distribution (Fig. S7), models AK135 and AK135+Crust1.0 have significant higher standard deviation than other models in 9-20 s period range, while in intermediate and long

period range, models S40RTS and S362ANI has significantly lower standard deviation. The systematic negative error still presents, except for model GyPSuM. The radial anisotropy feature of the contiguous U.S and surrounding regions are captured by models SEMum-NA14, Krischer18 and S362ANI. The travel time distribution of both SV and SH are more centralized with similar shape, while other models have a slightly systematically slower mean SH wave travel time. For the Love wave, we observe similar but much weaker feature compared to Rayleigh wave (Figs. S6 and S8), which indicates the radial anisotropy in the mantle for the contiguous U.S and surrounding regions still need further refinement. We also analyze the misfit functions for body and surface waves separately in Fig. S9 and S10. The misfits are generally similar to the overall misfits, while the surface wave misfits are larger, indicating the surface waves, especially in short periods, are not well fitted by current models. For specific models, for body wave in short period, models S362ANI, S40RTS and US-SL-2014 are top ranked in terms of smaller travel time and NZCC misfits. In longer period range (20-120 s), S40RTS, S362ANI and US.2016 outperforms others. For surface waves, models S40RTS, S362ANI and US.2016 are generally performs better in terms of travel time and NZCC misfits.

Text S5 We analyze the compatibility of crustal model and mantle model with the measurement of misfit functions and percentage of NZCC. Fig. 6 in the main text is the waveform comparison of a single station of the 200802211416A Nevada earthquake event (Mw 6.0). The epicentral distance is 18°.The models compared are S40RTS+Crust1.0, S40RTS+Crust2.0 and S40RTS+US.2016. Model US.2016 are also compared as a reference. We noticed that model S40RTS with Crust2.0 has slightly better waveform fitting compared to S40RTS with Crust1.0, indicating that Crust2.0, which is used as crustal correction in the model inversion process, is more compatible with the mantle model S40RTS. Even though Crust1.0 is a higher resolution crustal model, it may not as compatible as the original crustal model used in the inversion. S40RTS+US.2016 has a visible improvement on the Rayleigh waveform fitting in the Z and R direction, indicating that a non-compatible crustal model still has advantage to be combined with a mantle model. The high-NZCC percentage showing a similar trend that in short period range, S40RTS+US.2016 has higher percentage of high-similar waveforms for shear wave and Rayleigh wave. However, in longer period range, S40RTS+Crust2.0/Crust1.0 performs better (Fig. S11). The travel time misfit and NZCC misfit manifest similar feature (Fig. S12). In general, the variation of NZCC percentage and misfit in longer period (greater than 20 s) are small, therefore mantle model S40RTS combined with different crustal models (Crust1.0, Crust2.0 and US.2016) are almost at the same level in terms of waveform

predictability. Especially, the newly published global 3D FWI model (GLADM25, Lei et al., 2020) and model US.2016 are at the same level as different combinations of S40RTS and crustal models according to our test.

Text S6 We apply 1-D attenuation from PREM for mantle elements and a constant Q=600 in the crust. We examine the waveform example and misfit functions of the applied Q model and PREM 1-D Q model on S40RTS with Crust1.0, and the PREM 1-D Q model and 3-D Q model QRF12 on S362ANI in Fig. S13 and S14. The 3D Q model QRF12 is compatible with S362ANI than 1D PREM Q model. For the model S40RTS, there is a very slightly difference between 1D PREM Q model and the Q model we applied.

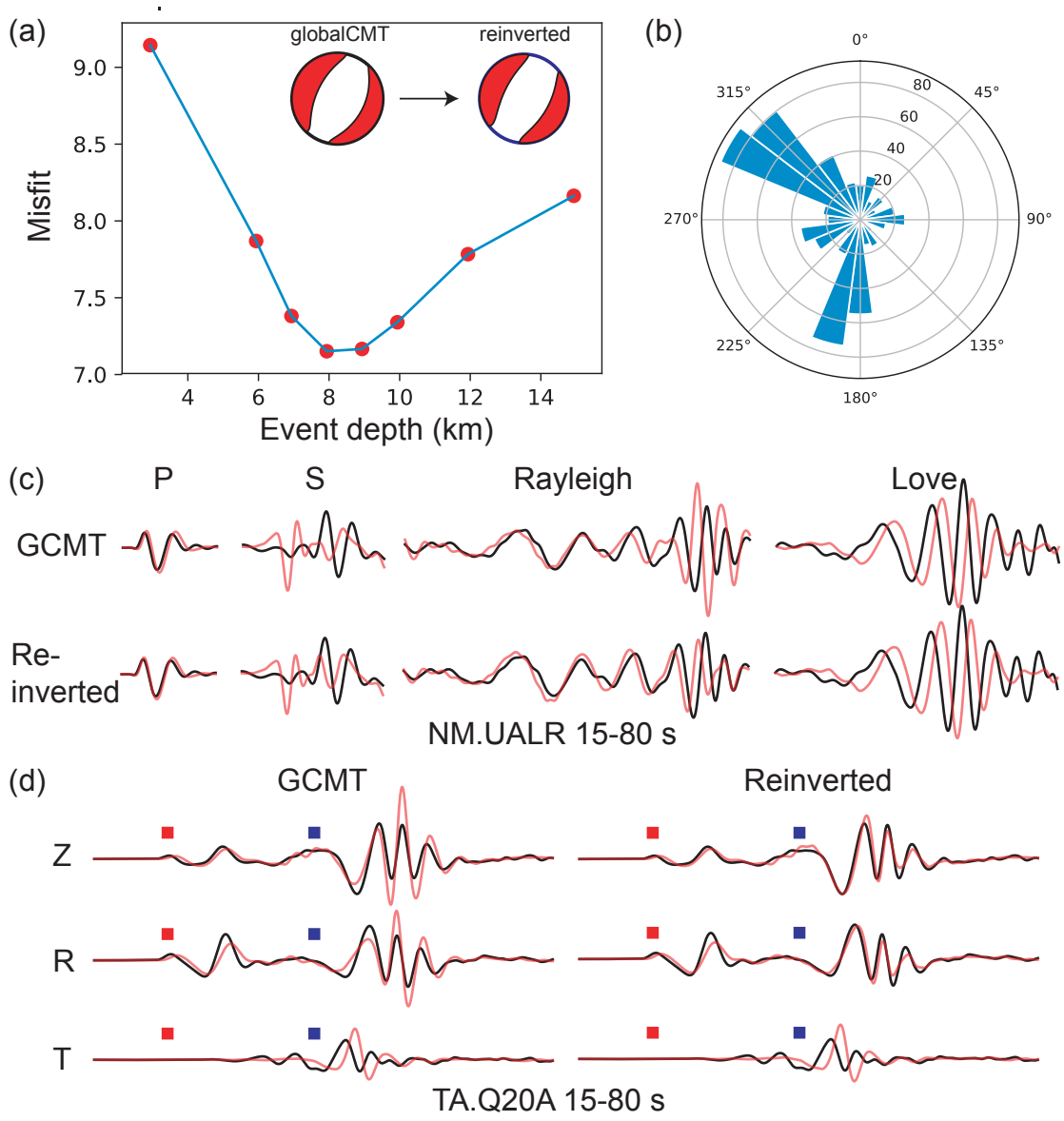

Figure S1. Example of earthquake source parameters re-inversion. (a) misfit function with event depth; (b) azimuthal bins and numbers of measurements in each azimuthal bin; (c,d) waveform examples of the original and re-inverted earthquake event parameters.

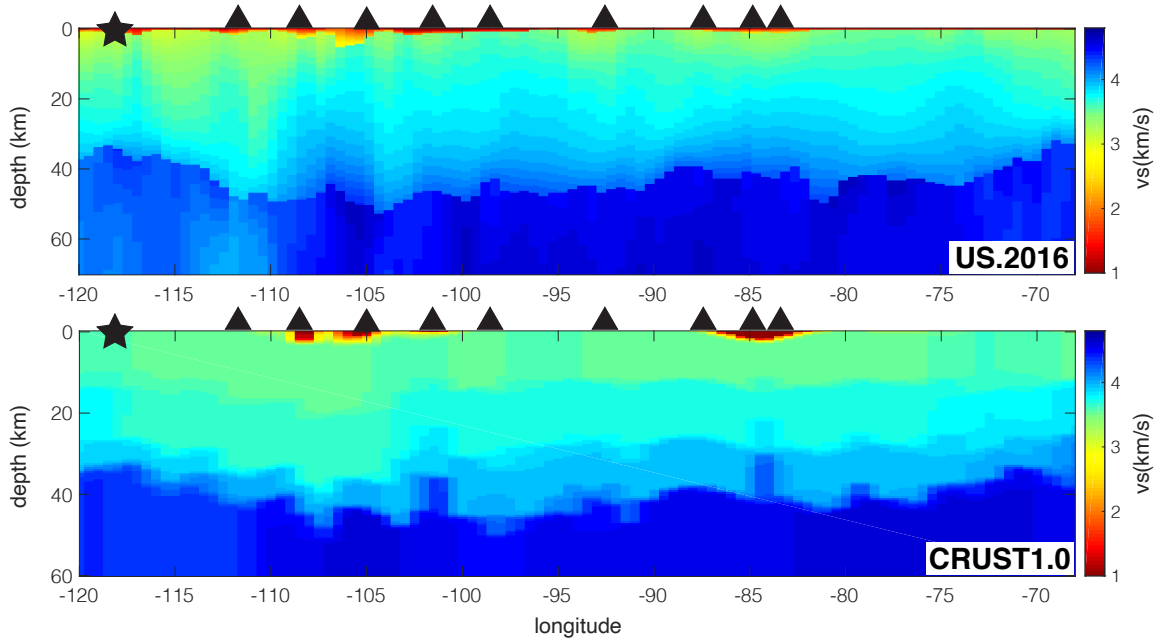

Figure S2. Cross section of the averaged shear wave velocity along 40°E within 1 degree perpendicular to the profile of models US.2016 and CRUST1.0. Star is showing the earthquake 201305240347A and triangles are showing the projection of the stations in Fig. 3c.

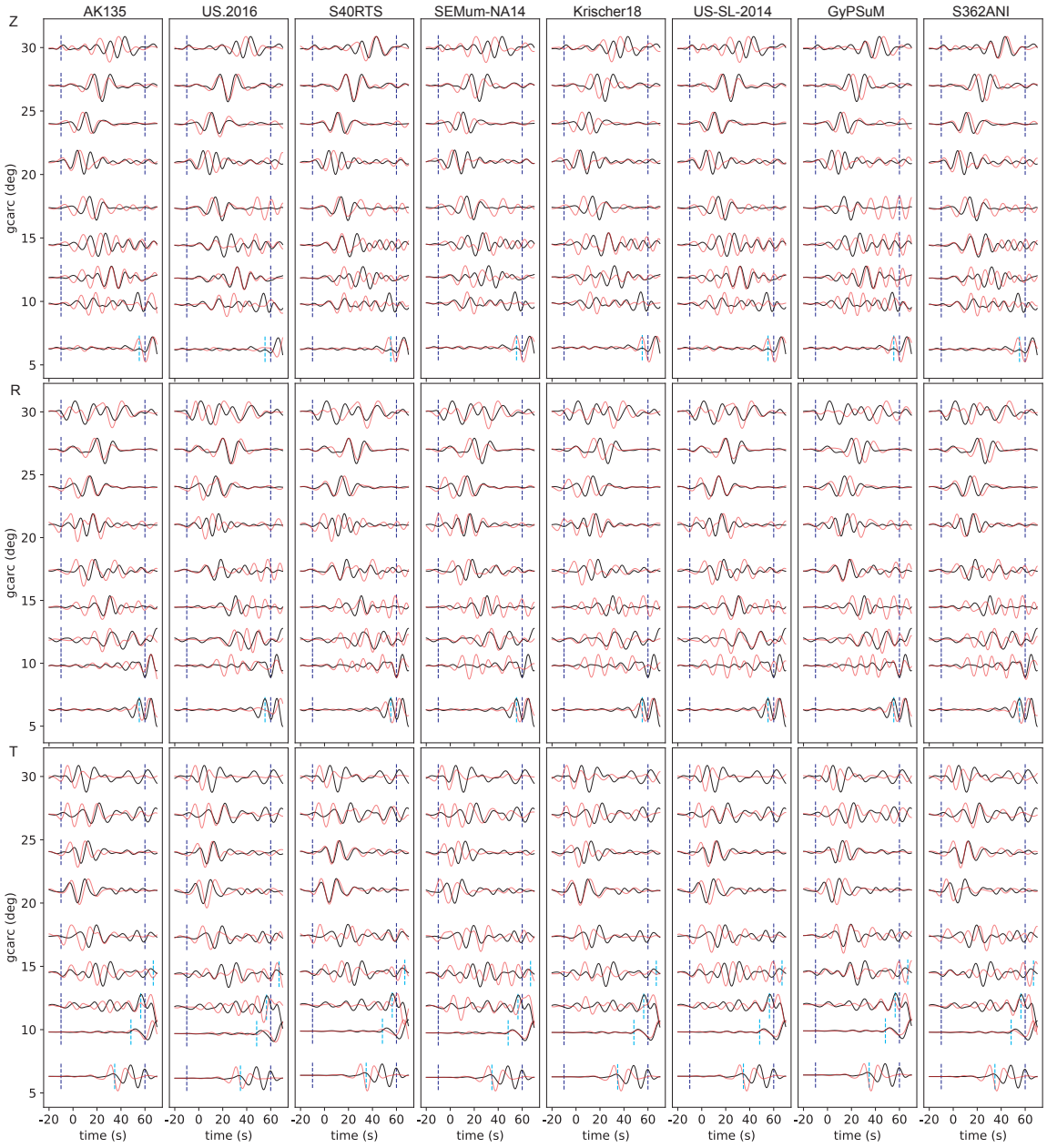

Figure S3. Waveform comparison for short period body waves. The seismic recordings are filtered between 9–20 s and aligned by the reduce time of the S wave arrival predicted by AK135. Black and red lines are the data and synthetics, respectively. Blue dashed lines mark the shear wave windows and cyan lines mark the starting point of the surface wave predicted by empirical Rayleigh and Love phase speed in Table 2.

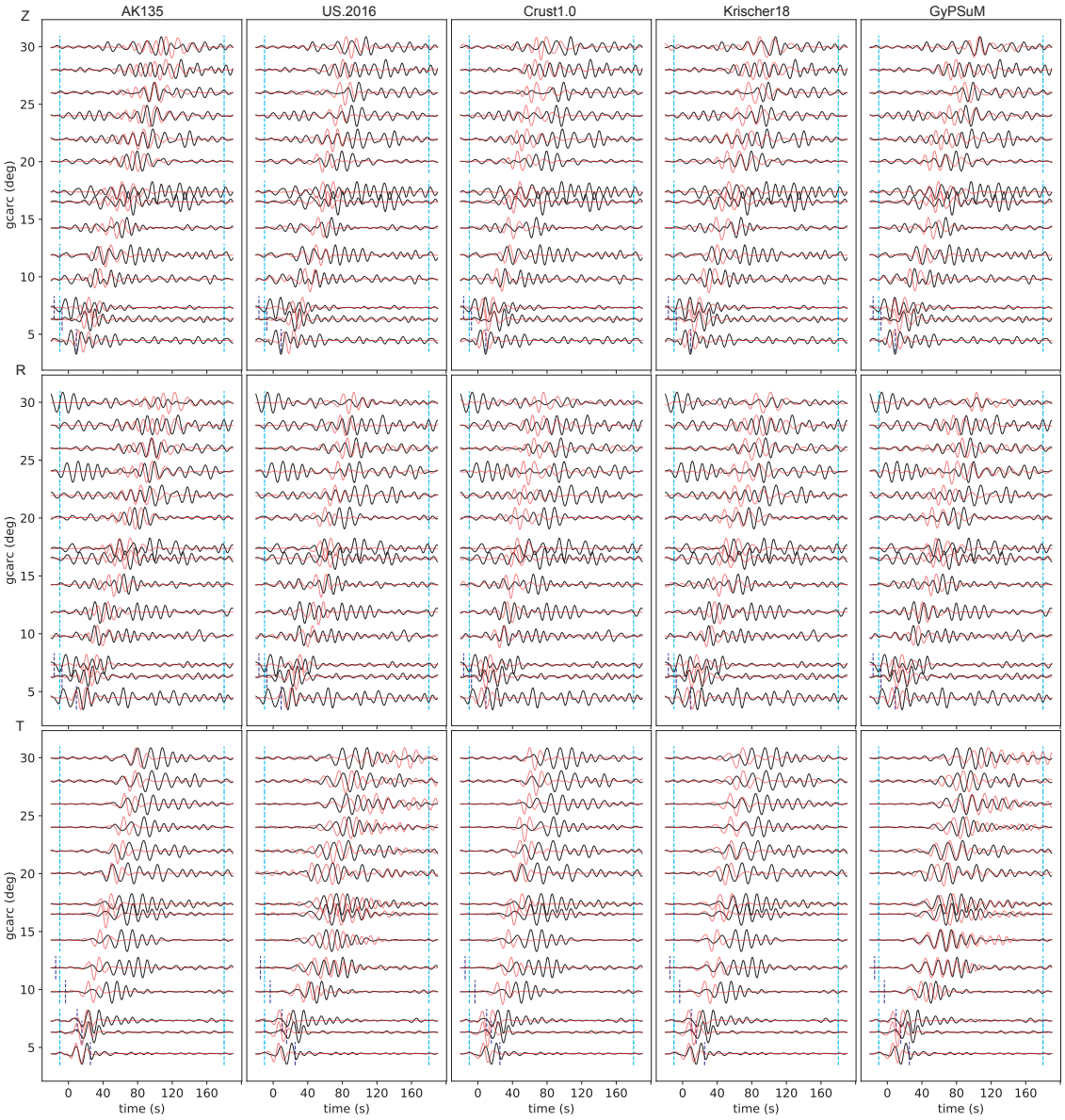

Figure S4. Waveform comparison for short period surface wave. The seismic recordings are filtered between 9–20 s and aligned by the empirical arrival time of Rayleigh or Love waves predicted by phase speeds in Table 2. Black and red lines are the data and synthetics, respectively. Cyan dashed lines mark the surface wave measurement window. Blue dashed line indicates the end of S wave window that is 60 s after S arrival predicted by AK135.

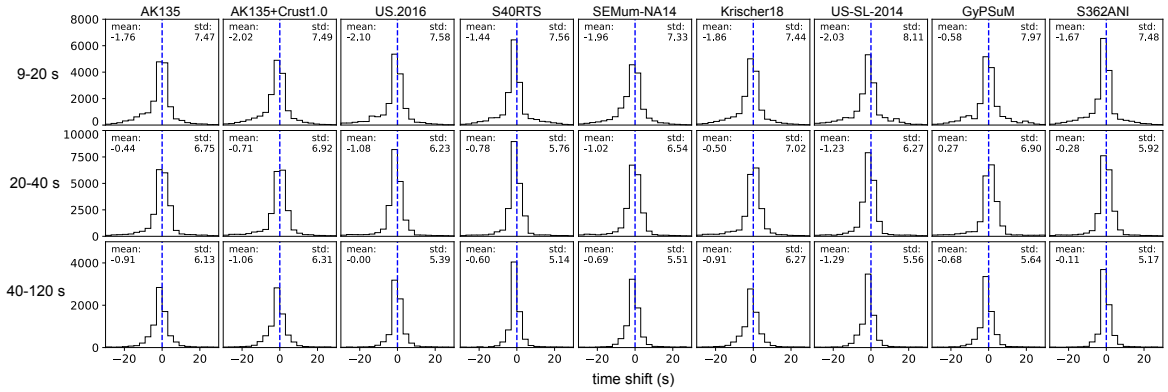

Figure S5. Travel time shift distribution histograms for body wave only measurement windows. Rows upper to lower: 9-20 s, 20-40 s and 40-120 s; Panels left to right: different models.

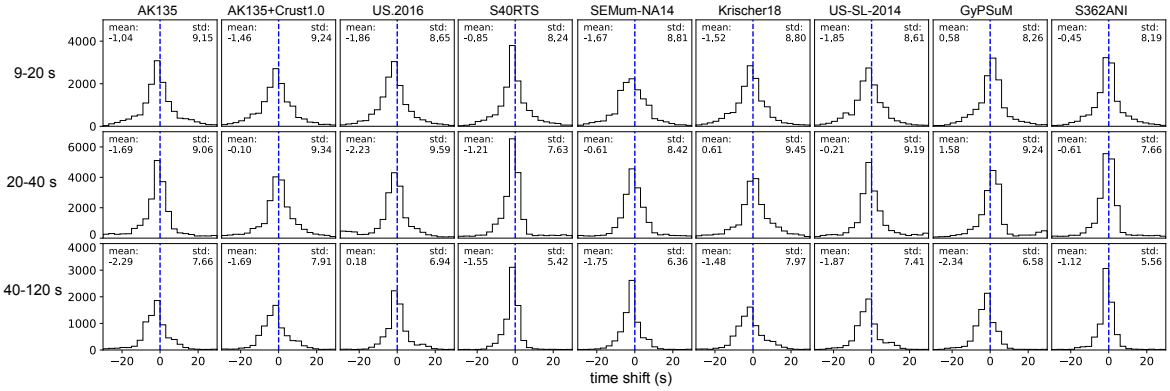

Figure S6. Travel time shift distribution histograms for SV and SH waves. Black and red lines and texts are for SV and SH, respectively. Rows upper to lower: 9-20 s, 20-40 s and 40-120 s; Panels left to right: different models.

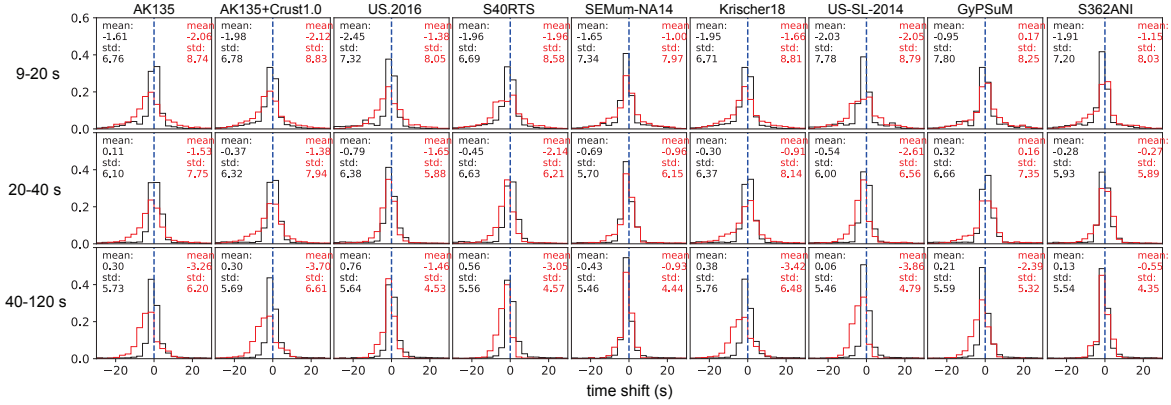

Figure S7. Travel time shift distribution histograms for surface wave only measurement windows. Rows upper to lower: 9-20 s, 20-40 s and 40-120 s; Panels left to right: different models.

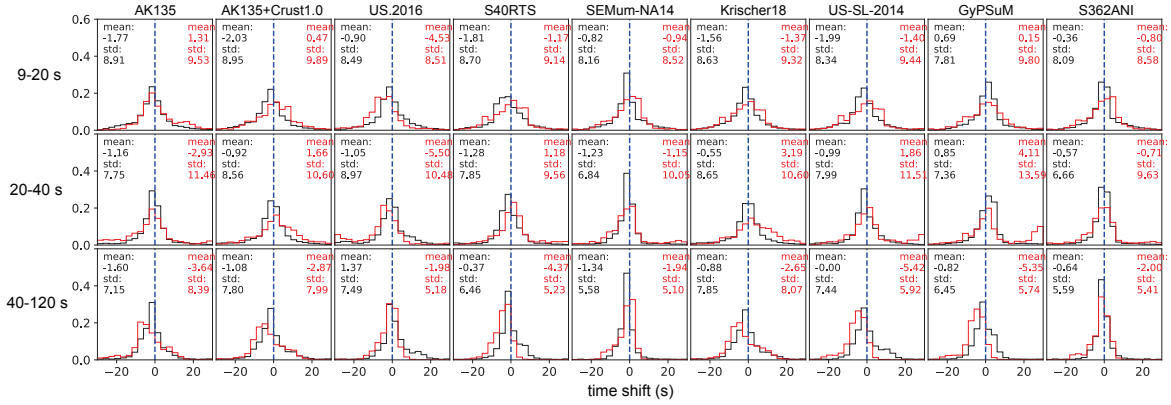

Figure S8. Travel time shift distribution histograms for Rayleigh and Love waves. Black and red lines and texts are for Rayleigh and Love, respectively. Rows upper to lower: 9-20 s, 20-40 s and 40-120 s; Panels left to right: different models.

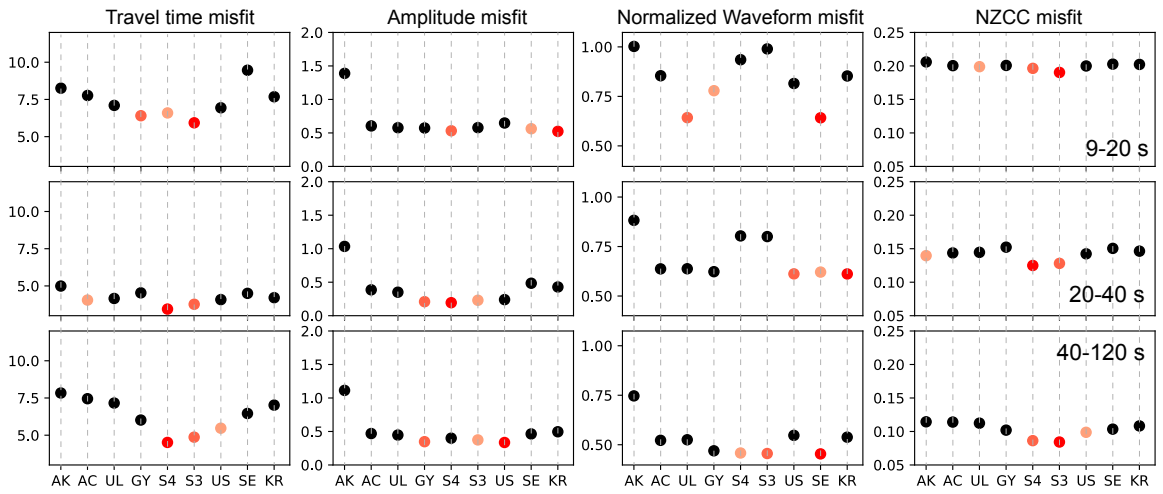

Figure S9. Misfit functions for body wave only. Rows upper to lower: 9-20 s, 20-40 s and 40-120 s; Columns left to right: different misfit functions.

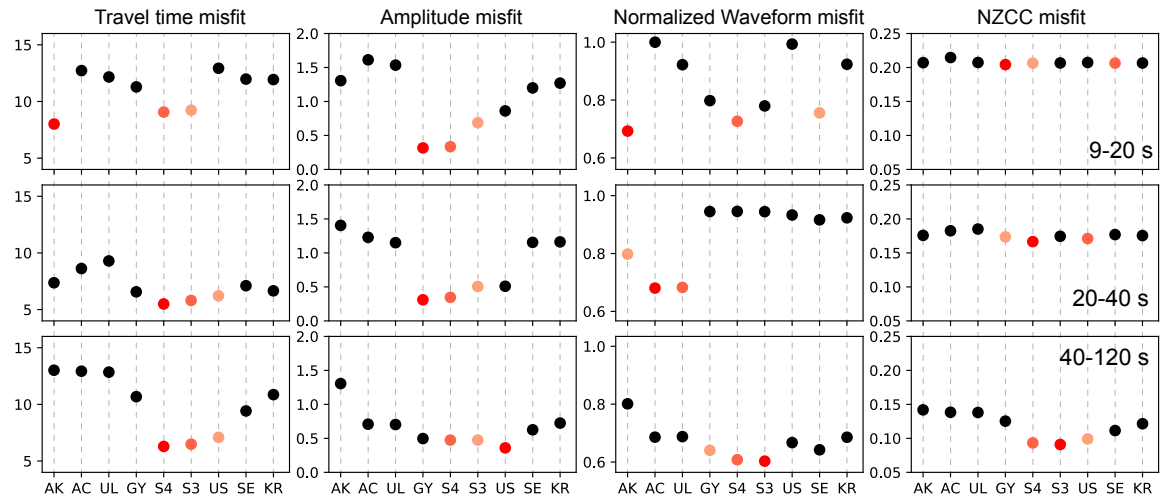

Figure S10. Misfit functions for surface wave only. Rows upper to lower: 9-20 s, 20-40 s and 40-120 s; Columns left to right: different misfit functions.

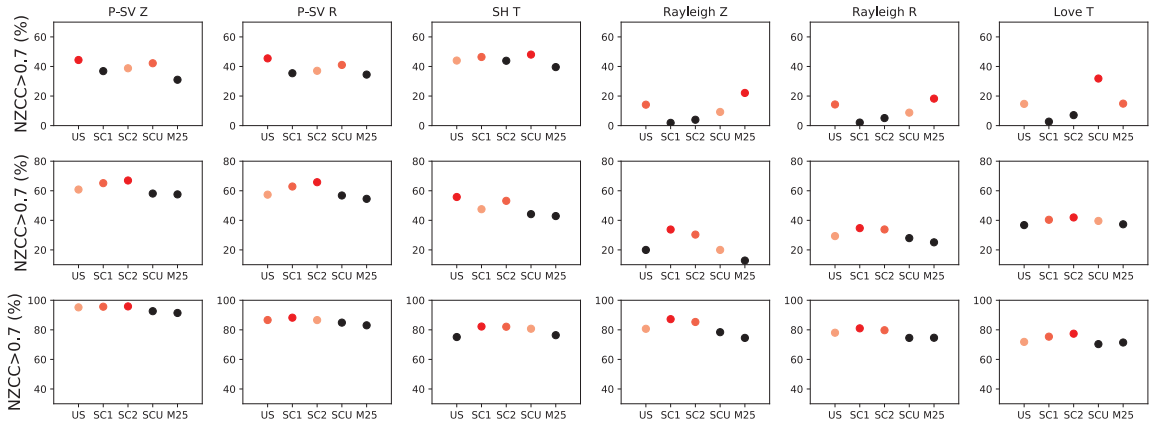

Figure S11. Percentage of NZCC> 0.7 of mantle model S40RTS with crustal model Crust2.0, Crust1.0, and US.2016, and model GLADM25 and US.2016 as references. From top to bottom lines are 9-20 s, 20-40 s and 40-120 s frequency range, respectively. From left to right column are different phases in different components, respectively.

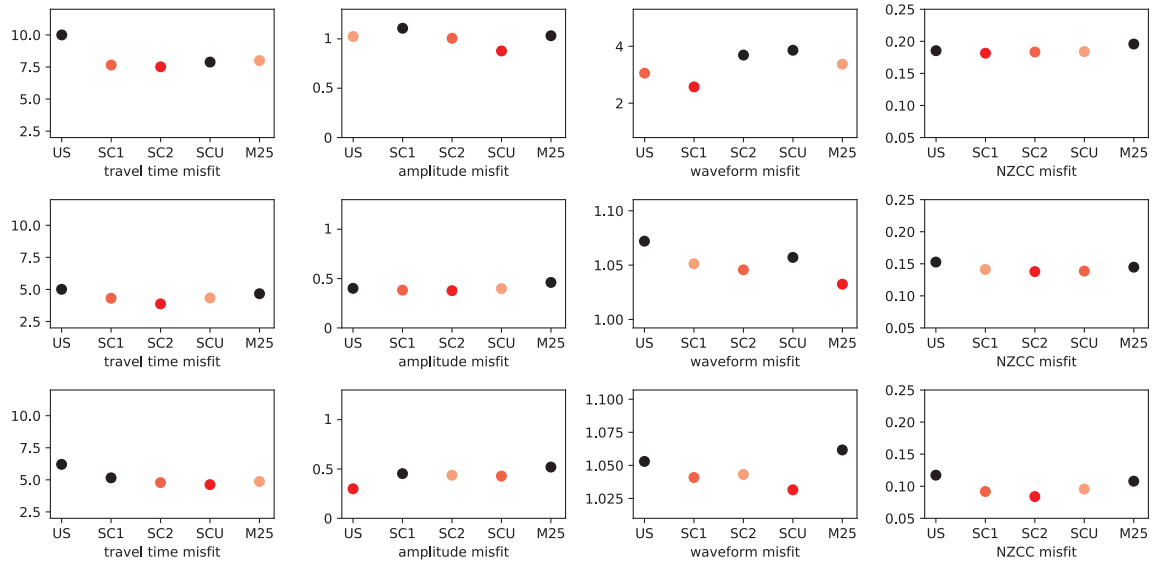

Figure S12. Misfit functions of mantle model S40RTS with crustal model Crust2.0, Crust1.0, and US.2016, and model GLADM25 and US.2016. From top to bottom lines are 9-20 s, 20-40 s and 40-120 s frequency range, respectively. From left to right column are travel time misfit, amplitude misfit, waveform misfit and NZCC misfit, respectively.

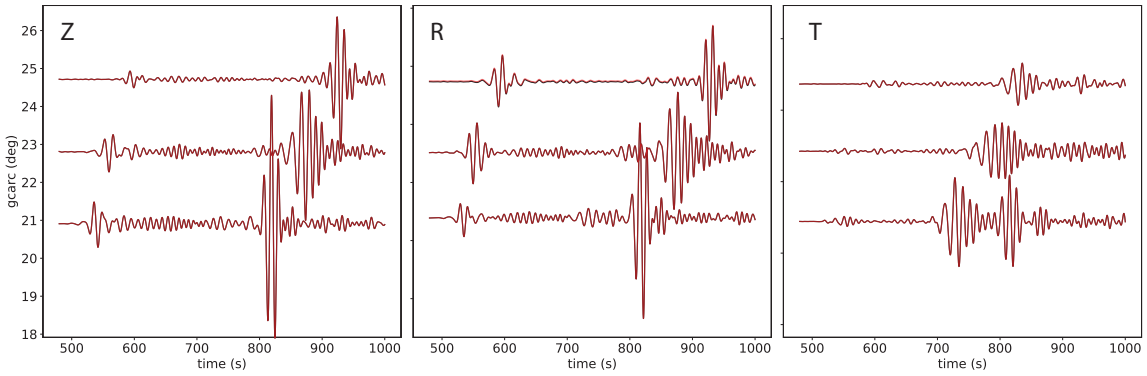

Figure S13. Waveform comparison of model S40RTS plus Crust1.0 in different Q models. Black: with 1D Q from PREM; Red: with constant Q=600 in the crust and PREM Q in mantle. Event: 200802211416A, station: IU.CCM. Epicentral distance: 17.9°. Waveforms are filtered to 20-40 s.

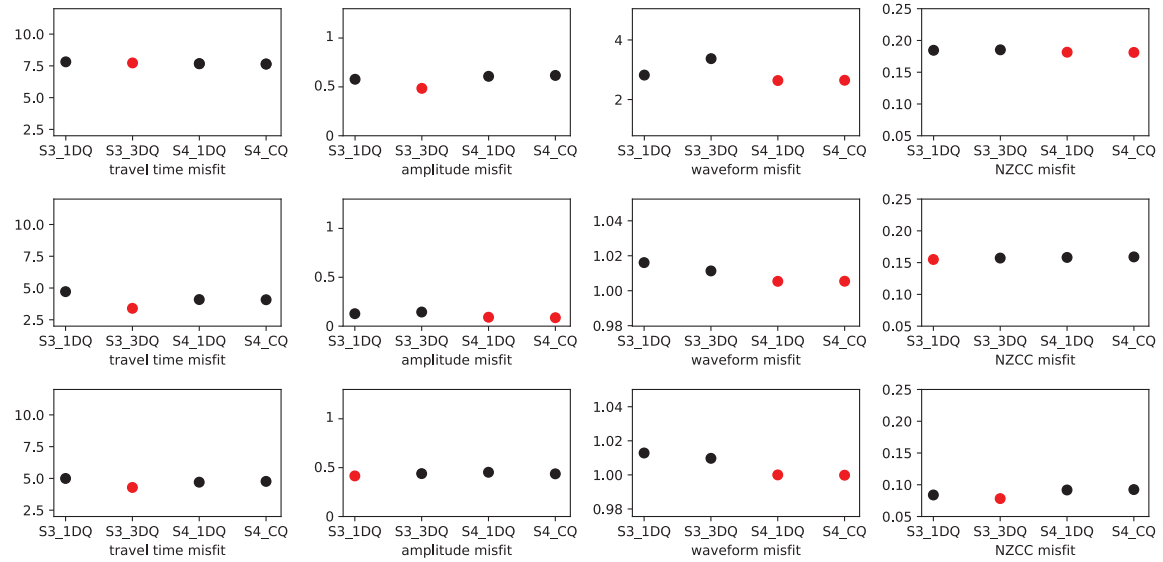

Figure S14. Misfit functions of model S362ANI and S40RTS plus Crust1.0 in different Q models. From top to bottom lines are 9-20 s, 20-40 s and 40-120 s frequency range, respectively. From left to right column are travel time misfit, amplitude misfit, waveform misfit and NZCC misfit, respectively.

REFERENCES

Coleman Jr, J. L. & Cahan, S. M., 2012. Preliminary catalog of the sedimentary basins of the united states.

Ekström, G., Nettles, M., & Dziewoński, A., 2012. The global cmt project 2004–2010: Centroid-moment tensors for 13,017 earthquakes, *Physics of the Earth and Planetary Interiors*, **200**, 1–9.

Jia, Z., Ni, S., Chu, R., & Zhan, Z., 2017. Joint inversion for earthquake depths using local waveforms and amplitude spectra of rayleigh waves, *Pure and Applied Geophysics*, **174**(1), 261–277.

Liu, Q., Polet, J., Komatitsch, D., & Tromp, J., 2004. Spectral-element moment tensor inversions for earthquakes in southern california, *Bulletin of the Seismological Society of America*, **94**(5), 1748–1761.

Zhu, L. & Helmberger, D. V., 1996. Advancement in source estimation techniques using broadband regional seismograms, *Bulletin of the Seismological Society of America*, **86**(5), 1634–1641.